THE UNIVERSITY OF ALBERTA

DYNAMICS OF BAROCLINIC WAVES

AND BLOCKING RIDGE DEVELOPMENT

by

(C) LAWRENCE WAYNE DIEHL

A THESIS

SUBMITTED TO THE FACULTY OF GRADUATE STUDIES AND RESEARCH

IN PARTIAL FULFILMENT OF THE REQUIREMENTS FOR THE DEGREE

OF MASTER OF SCIENCE

IN

METEOROLOGY

DEPARTMENT OF GEOGRAPHY

EDMONTON, ALBERTA

FALL, 1977

Dedicated to
my loving wife and children

ABSTRACT

In this study a linear two-level baroclinic model is
formulated in which the zonal steady-state current is
perturbed by surface friction and surface sensible heat
exchange. The perturbation quantities are assumed to be
either independent of latitude or varying sinusoidally with
latitude.

Investigation of the phase velocity response of the
model indicates that sensible heat exchange decreases the
amount of instability of short and intermediate waves, but
increases the longwave instability. The combined influence
of friction and diabatic heating is to create unstable long
waves which travel eastwards at reduced speeds and which may
be stationary or retrogressive in nature depending on the
speed of the mean zonal current.

Phase and amplitude characteristics of the existing
perturbation waves suggest that the thermal wave necessarily
lags the geopotential wave during amplification while the
static stability wave prefers a lead position. In addition,
maximum downward vertical velocity and maximum surface
sensible heat transfer to the atmosphere occur between the
ridge and downstream trough position.

It has been suggested that blocking ridges may be a
form of longwave baroclinic instability and that sensible
heat transfer plays an important role in their formation.
Comparison of numerical predictions of unstable longwave

amplification with observed North Pacific blocking space and time scales indicates that without the presence of sensible heating in the model the development of blocking waveforms is not feasible. With sensible heat exchange stationary unstable waveforms are obtained which have growth times and wavelengths that are similar to observed North Pacific blocks.

ACKNOWLEDGEMENTS

TABLE OF CONTENTS

Page

LIST OF TABLES

LIST OF FIGURES

CHAPTER 1

INTRODUCTION

1.1 Theories on Blocking-Ridge Formation

Blocking-ridge activity is one of the most visible
forms of longwave growth in the atmosphere and has long been
recognized as being a major influence on regional climate.
Such enduring ridge formations, which are found to be more
frequent and pronounced during the winter, can displace
passing synoptic disturbances considerable distances to the
north or south of normal storm tracks. This then invariably
leads to anomalies in such parameters as surface temperature
and precipitation when compared to the non-blocking regime.
Although the climatic effects and behavior of blocking
ridges have been well documented, the dynamic causes
surrounding their initial formation and development are
still not fully understood.

In an early consideration of blocking phenomena, Yeh
(1949) suggested that the transfer of energy by dispersive
waves in the atmosphere might explain the occurrence of
sustained ridging. These waves are created by a process of
rapid adjustment between the pressure and velocity fields
and energy propagation occurs at a group velocity which can
be very different from the speed of the prevailing westerly

current. By examining the characteristics of a solitary
wave within an incompressible uniform atmosphere, it was
shown that once a pressure rise or fall was created near the
pole it would remain there without being dispersed. At
latitudes other than the pole the solitary pressure wave was
found to retrogress while slowly spreading out and
dispersing, a characteristic often exhibited by atmospheric
blocks. From these results it was concluded that blocking
activity was likely a high-latitude feature of atmospheric
flow which has greater intensity, a longer lifetime and
moves with slower velocities as latitude increases.

Although this concept can describe a few of the
prominent properties of the blocking process it represents
others inaccurately. For instance it overpredicts both the
extent of the motion and the rate of dispersion of blocking
ridges at lower and middle latitudes. Figure 1.1
illustrates the behavior of a solitary dispersive wave at
40N and 70N. The curve representing the theoretical results
for 40N shows that after a relatively brief period of 32
hours the wave amplitude has dropped to 1/3 of its initial
value and has moved upstream more than 6000 km. At 70N
after two days the same solitary wave had retrogressed at an
average speed of 880 km/day and its amplitude had diminished
by approximately 1/6 of its original value. The
characteristics of the wave at 40N are not representative of
actual blocking behavior, while the wave speed and
dispersion rate at 70N are more indicative of the last
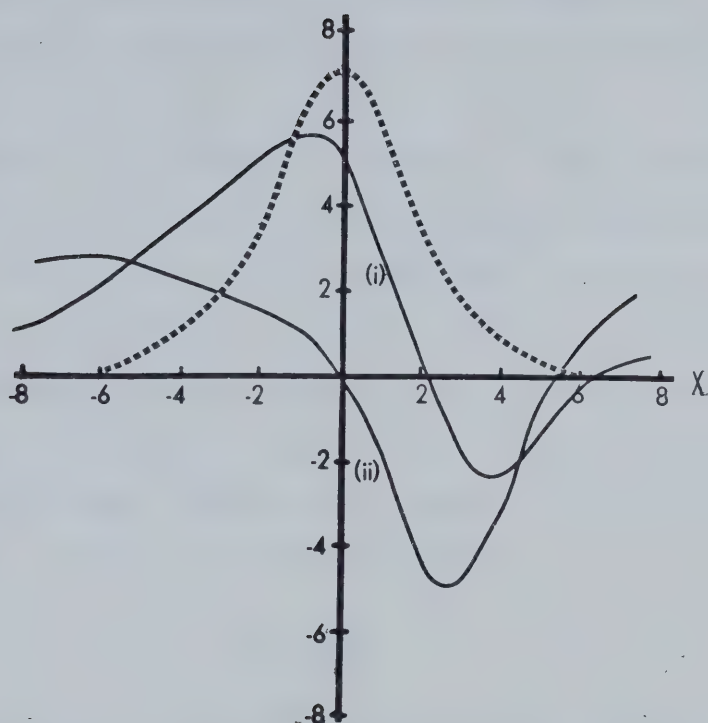
Fig. 1.1. Dispersion of an initial solitary wave. The dashed curve is the initial waveform at time t = 0; curve (i) is the wave profile at latitude 40N after approximately 32 hours and curve (ii) is the wave profile as seen at 70N after approximately 2 days. The abscissa is in units of 2200 km, while the ordinate is in arbitrary non-dimensional units of amplitude. The rate of dispersion of the wave amplitude at both latitudes increased significantly as time progressed. The speed of the retrogression at 70N remained constant, however, accelerated retrogression was observed at 40N as time went on. Curves are taken from Yeh (1949).

stages of blocking when the ridge is deteriorating.   In
general the theory does not describe satisfactorily the
development or persistence aspects of the phenomenon nor
does it explain why atmospheric blocks tend to show a
longitudinal and seasonal preference in their formation.

Other investigators such as Berggren, Bolin and Rossby
(1949) have hypothesized that blocking in the form of a
wave-like perturbation could be analogous to that of a
hydraulic jump in open channel flow.   Continuing this
approach, Rex (1950a) employed a hydraulic analogue model as
devised by Rossby (1950) and a momentum transfer argument to
arrive at a critical velocity given by

$$u_c = \beta \frac{a^2}{3} \qquad\qquad (1.1.1)$$

where β is the linear Beta-plane approximation to the north-
south variation in the Coriolis parameter f
(i.e. $f(y)=f_o + \beta y$), and a is the half-width of the current
flow.   Whenever the actual zonal current speed exceeds u
two permissible modes of flow exist with one being at a
higher energy level and velocity than the other; a necessary
condition for an analogy to a hydraulic jump.   From (1.1.1)
it is evident that decreasing the stream width and
increasing its flow speed meant lowering the critical
threshold of the flow such that an external impulse to the
stream might cause the jump to a higher energy state.
Therefore a region aloft with a narrow strong jet and
anomalously low thickness values (shallow stream depth)

would lend itself more easily to the formation of a blocking ridge. The propagation of the atmospheric 'jump' once it has formed was determined to be

$$c = N - n(n+1) \qquad (1.1.2)$$

where $N=u/u_c$ is the critical velocity ratio, u is the immediate upstream current velocity, and $n=a_1/a$ is the expansion ratio of the upstream and downstream current half-widths as indicated in Figure 1.2.

After applying the theory to a number of test cases, Rex (1950a) concluded that no major contradictions were apparent and that the concept gave credible results in predicting when blocking might occur. However, one argument made against the hydraulic jump theory is that it lacks a feasible energy source required to excite and then maintain the developed wave state associated with occurrences of blocking in the atmosphere. There is also some question as to how applicable the idea of a finite current width is to the real atmosphere. In narrow 'well-defined' stream widths when the term a is small, calculations of u are apt to be unrealistically small and the resulting inordinately large values of N and n do not lead to the correct interpretation of blocking behavior. In situations when the flow boundaries are not so well-defined there is often some arbitrariness in the selection of the half-width and therefore some uncertainty about the value of the predictions.
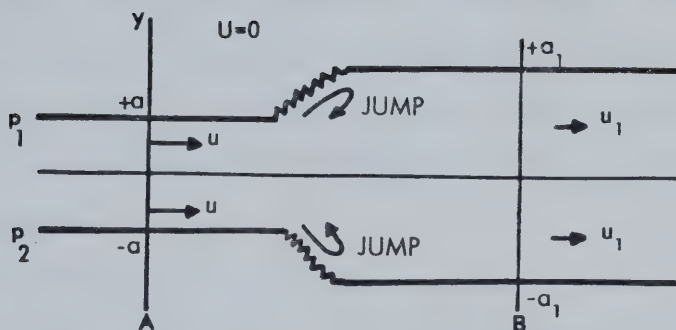
Fig. 1.2. The simple two-dimensional steady current envisioned in the hydraulic jump analogue model used by Rex (1950a). Zonal current speed u is assumed constant over the cross-section A, as is u_1 over cross-section B. The "jump" can occur according to the theory if $N = u/u_c > 1$, where the critical velocity is defined as $u_c = \beta a^2/3$. Current flow is assumed to vanish (U = 0) in the environment surrounding the channel.

In an investigation of the zonal index cycle, Namias (1950) alluded to the possiblity that blocking action was a manifestation of baroclinic instability in the atmosphere. Later, after studying the interactions of an ocean-atmosphere environment, Namias (1959) proposed that the thermal energy anomalies contained in the upper ocean may provide the necessary energy source for occurrences of mid-ocean blocking. Other studies on sea-atmosphere heat

transfers, however, have indicated that fluctuations in the ocean's surface temperature do not normally play an active role in governing thermal energy exchanges on a time scale such as is associated with the development of blocking ridges (Kraus and Morrison,1966; Clark,1967). It would seem that sensible heat transfer in response to surface air temperature fluctuations could form a more viable energy source having a suitable time scale of several days to several weeks.

Theoretical results which have been interpreted as supporting the baroclinic instability concept of blocking-ridge formation came from work done by Haltiner (1967). Using a linearized two-level baroclinic model he has indicated that with the input of sensible heating from the surface a region of possible stationary or retrograde unstable wave growth is created for longer wavelengths in the range of 7000-9000 km. The instability of long waves in general was found to increase gradually as the amount of sensible heating was increased while waves on a near-synoptic scale became slightly more stable. These results were obtained for representative 50 kilopascal level winter values at mid-latitudes.

Encouraged by this theoretical evidence, White and Clark (1975) examined monthly mean atmospheric data taken over the North Pacific covering a period of 1950-1970. Their study found that blocking action was most often observed over the North Pacific ocean at a longitude of 160W

to 170W with a dominant space scale of 6000 to 7000 km. In
addition they were to discover that the distribution of
anomalous surface sensible heat flux was strongly correlated
with the anomalous 70 kPa heights associated with the
development of blocking ridges. Below normal heating values
were found to occur under the position of the ridging and
above normal sensible heat exchange was associated with the
adjacent trough regions on either side of the block. It was
the conclusion of these investigators that sensible heat
exchange between the ocean and the atmosphere was likely
very important in the formation of blocking ridges and that
the application of baroclinic instability theory to this
type of phenomenon seemed plausible.

1.2 Two-level Baroclinic Models

Many of the baroclinic models which have been utilized
in numerical prediction are of a simple two-level design.
The procedure usually consists of applying a vorticity
equation at two isobaric levels in the modelled atmosphere,
(e.g. 25 kPa and 75 kPa) and a thermodynamic equation at an
intermediate level, (50 kPa). The sum and the difference of
the vorticity equations over the upper and lower information
levels constitute averaged and thermal equations,
respectively. The system of equations is then closed by an
equation of state. Analysis of the dynamics of the model is
possible by employing perturbation wave solutions with which
the equations are reduced to that of the linear type and a

frequency equation is obtained.

Early studies using this approach assumed that the motions in the atmosphere were both adiabatic and frictionless. Using a quasi-geostrophic linearized two-level model, Holopainen (1961) was able to incorporate the effects of surface friction into his perturbation equations. For adiabatic frictionless flow, using representative atmospheric values, it had been established that the perturbation field contained a unstable component over a small range of relatively short wavelengths. The effect of introducing surface friction was to broaden this range slightly while reducing the component amplitude of the previously-existing unstable wavelengths. Haltiner and Calverly (1965) using a similar formulation investigated the influence of surface-based friction on the interactions between the averaged wave and the thermal wave. Their study gave evidence that the phase characteristics of the two waves were markedly affected by friction. Results showed that decreases in the limiting phase difference were predicted when the value of the surface drag coefficient was increased.

Applying a different formulation of the hydrodynamic equations, Lorenz (1960) designed a two-level non-geostrophic model which allowed for full variability in the Coriolis parameter and the static stability. Gates (1961) has investigated the linearized form of this model under conditions of frictionless adiabatic flow. His results

suggested that the unstable perturbation component was
significantly larger using a variable static stability than
for cases in the usual quasi-geostrophic formulation when
this stability parameter was held constant. The
perturbation equations as derived in this study formed the
basis for the previously-mentioned investigation into
sensible heat influences on baroclinic instability by
Haltiner (1967).

The dynamics of baroclinic waves have not been
investigated by analytical methods alone. Kikuchi
(1969,1971) used spherical harmonics for the time
integration of the vorticity and thermodynamic equations in
a quasi-geostrophic two-level model. These numerical
investigations were aimed directly at reproducing the
occurrence of blocking action and at gaining a better
understanding cf the effects of diabatic heating and
mountain ranges on the behavior of such longwave growth.
Included in the diabatic heating were the release of latent
heat and radiational flux divergence as well as sensible
heat exchange. Numerical computations showed that quasi-
stationary longwave amplification similar to blocking
processes occurred in the model whether orography was
included or not. The main effect of the inclusion of
mountains in the model was to lengthen slightly the duration
of the computed ridging and to create preferred longitudinal
regions where blocking occurred more frequently.

1.3 Intentions of This Study

In this study a two-level baroclinic model which incorporates a variable static stability will be developed. Terms which will describe the input of surface sensible heating as well as lateral and vertical turbulent heat flux in the atmosphere are included. The effects of introducing surface friction at the lower boundary of the atmosphere and those friction terms arising from turbulent diffusion by small eddies within the current flow will also be examined.

The governing equations will be linearized by neglecting squares and products of the perturbation variables. The dynamic features of the linear model will then be analyzed. The emphasis of this analysis will be on the stability of the baroclinic waves in response to varying values of sensible heating, friction and other variables as well as the interactions between perturbation waves.

Of particular interest, in view of the findings of White and Clark (1975), will be the behavior of the so-called long wavelengths in the possibility of explaining some aspects of blocking-ridge development. It cannot be expected, however, that any perturbation method will be able to portray accurately all of the characteristics of the longwave amplification we observe in the real atmosphere such as those found in the blocking process. One feature that may be difficult to explain by perturbation analysis is the persistence of blocks. After having gone through a period of unstable growth, the ridge can be seen to remain

in a non-amplifying developed state for an extended length
of time, implying that some form of stable mode is
accquired.   It seems likely that this is beyond the
prediction capability of a linearized model and, therefore,
what will be of prime concern in this study is the period of
time when instability is realized and wave amplitude
increases to a developed state.

CHAPTER 2

DEVELOPMENT OF THE MODEL

2.1 Consistency in Energy and Vorticity

In designing a simple baroclinic model some manner of
modification is required to reduce the system of
hydrodynamic equations to a less complicated form. In order
to yield what would still be considered compatible results
it is desirable that the reduced relations are consistent
with any conservation principles expressed by the exact
equations. The governing equations which describe
atmospheric motions exhibit several such principles
regarding the production of relative vorticity and energy on
a global basis. They are:

  (a) the mean generation of relative vorticity
      over a global pressure surface is zero;

  (b) total energy under reversible adiabatic
      processes is conserved; and

  (c) the sum of the kinetic energy and the
      available potential energy is conserved.

One method of simplifying a given equation is to
compare the magnitudes of the various terms within it and
then neglect those which are of smaller order. The orders
of magnitude of individual terms are based on time and space
scale considerations of the phenomenon to which the equation

13

is being applied. This approach is therefore called scale analysis and was introduced by Charney (1948). Application of the scale analysis technique while checking to maintain the integral vorticity and energy invariants allows the governing equations to be reduced in a consistent manner.

A reduction in the complexity of the equations can also be made by using some form of general approximation pertaining to the atmospheric velocity field. The type of approximation used in many models is the quasi-geostrophic assumption in which the horizontal velocity field and vertical component of relative vorticity are evaluated by the non-divergent geostrophic wind. Charney (1947) has shown that assuming the horizontal velocity to be geostrophic has the effect of filtering out high-speed inertia-gravitational waves which occur in the equations of motion and thereby a significant simplification is achieved. The conventional quasi-geostrophic two-level baroclinic model (Charney and Phillips,1953), however, has inherent energetic inconsistencies which result in prediction errors. For example, there is a tendency for the model to over-predict the amount of kinetic energy in the atmosphere. Such inconsistencies and their effect on the model's performance are discussed by Gates (1961).

A simplified set of dynamic equations which possesses certain consistent integral properties with respect to energy and vorticity has been formulated by Lorenz (1960). For a filtering approximation the quasi-geostrophic

assumption was replaced by a relation known as the balance equation. This approximation is derived from the following form of the divergence equation

$$\nabla^2 \phi - f \mathcal{S} + \left(\hat{k} \times \vec{V} \right) \cdot \vec{\nabla} f - 2 J(u,v) = 0 \qquad (2.1.1)$$

where is the geopotential, $\vec{V}$ is the horizontal wind for which u is the west-east x-component and v the south-north y-component, $\vec{\nabla} = \hat{i} \, \partial/\partial x + \hat{j} \, \partial/\partial y$, $\mathcal{S} = \vec{\nabla} \times \vec{V}$ is the vertical component of relative vorticity, $\hat{i}$, $\hat{j}$ and $\hat{k}$ are the unit vectors and $\bar{J}$ represents a Jacobian in the normal differential form. If a stream function ψ and a velocity potential χ are defined such that

$$\vec{V} = \vec{V}_{\psi} + \vec{V}_{\chi} \qquad (2.1.2)$$
$$\vec{V}_{\chi} = \vec{\nabla} \chi \qquad (2.1.3)$$
$$\vec{V}_{\psi} = \hat{k} \times \vec{\nabla} \psi \qquad (2.1.3)$$

in which $\vec{V}_{\psi}$ and $\vec{V}_{\chi}$ are the rotational and divergent portions of the horizontal wind, then (2.1.1) takes the form

$$\nabla^2 \phi - \vec{\nabla} \cdot \left(f \vec{\nabla} \psi \right) + 2 \left(\frac{\partial^2 \psi}{\partial x \partial y} \right)^2 - 2 \frac{\partial^2 \psi}{\partial x^2} \frac{\partial^2 \psi}{\partial y^2} = 0 \qquad (2.1.5)$$

Thus the balance equation as given by by (2.1.5) implies that a continual equilibrium exists between the rotational portion of the wind and the geopotential field.

The prognostic equations used with (2.1.5) were the adiabatic thermodynamic equation and the vorticity equation neglecting friction. The former can be expressed as

$$\frac{d\theta}{dt} = \frac{\partial\theta}{\partial t} + \vec{V}\cdot\vec{\nabla}\theta + \omega\frac{\partial\theta}{\partial p} \qquad (2.1.6)$$

where ω =dp/dt represents vertical velocity, t is time and θ the potential temperature. Potential temperature at a given pressure p (kPa) and temperature T ($^{\circ}$C) is given by the relation

$$\theta = \left(\frac{100}{p}\right)^{\chi} T \qquad (2.1.7)$$

in which k =R/c_p is a dimensionless ratio of the specific gas constant of dry air R and the specific heat capacity of air at constant pressure c_p.

The version of the vorticity equation which was used can be written as

$$\frac{\partial f}{\partial t} + \vec{V}\cdot\vec{\nabla}\left(f+f\right) + \omega\frac{\partial f}{\partial p} + \left(f+f\right)\vec{\nabla}\cdot\vec{V}_x + \hat{k}\,\vec{\nabla}\omega \times \frac{\partial\vec{V}_\psi}{\partial p} = 0 \quad (2.1.8)$$

By applying (2.1.2)-(2.1.4) relative vorticity can be related to the stream function by

$$f = \vec{\nabla}\times\vec{V} = \vec{\nabla}\times\vec{V}_\psi = \nabla^2\psi \qquad (2.1.9)$$

In addition if δ represents horizontal divergence $\vec{\nabla}\cdot\vec{V}$, then

$$\delta = \nabla\cdot\vec{V}_x = \nabla^2\chi \qquad (2.1.10)$$

Therefore, under hydrostatic conditions defined by

$$\frac{\partial\phi}{\partial p} = -\frac{1}{\rho} \qquad (2.1.11)$$

where ρ is density, the continuity equation can be written in the following form

$$\delta + \frac{\partial \omega}{\partial p} = \nabla^2 \chi + \frac{\partial \omega}{\partial p} = 0 \qquad (2.1.12)$$

Employing (2.1.2)-(2.1.4), (2.1.9) and (2.1.12) the prognostic equations (2.1.6) and (2.1.8) can be written as

$$\frac{\partial \theta}{\partial t} + J(\psi, \theta) + \vec{\nabla}(\theta \vec{\nabla}\chi) + \frac{\partial}{\partial p}(\omega \theta) = 0 \qquad (2.1.13)$$

$$\frac{\partial}{\partial t} \nabla^2 \psi + J(\psi, \nabla^2 \psi + f) + \vec{\nabla}\chi \cdot \vec{\nabla}(\nabla^2 \psi + f) + \omega \frac{\partial}{\partial p} \nabla^2 \psi$$
$$+ (\nabla^2 \psi + f)\delta + \vec{\nabla}\omega \cdot \vec{\nabla}\frac{\partial \psi}{\partial p} = 0 \qquad (2.1.14)$$

Through a systematic analysis of the integral constraints, Lorenz (1960) has shown that together (2.1.5) and (2.1.14) have invariant energy and vorticity relations similar to the exact divergence and vorticity equations. Thus, with the addition of (2.1.13), they form an energetically-consistent system of equations.

This system of equations can be reduced further if the phenomenon to which the motions are being applied is of a synoptic or larger scale. After (2.1.14) is subjected to such a scale analysis (cf Haltiner,1971) and smaller terms are omitted, a second approximation which maintains the integral vorticity constraint is

$$\frac{\partial}{\partial t} \nabla^2 \psi + J(\psi, \nabla^2 \psi + f) + \vec{\nabla}\chi \cdot \vec{\nabla}f - f\frac{\partial \omega}{\partial p} = 0 \qquad (2.1.15)$$

An equation originating from (2.1.5) which, when used with (2.1.15), satisfies the energy constraints is

$$\nabla^2 \phi - \vec{\nabla}f \cdot \vec{\nabla}\psi - f\nabla^2 \psi = 0 \qquad (2.1.16)$$

Equation (2.1.16) is sometimes called the 'linear' balance
equation. The set of equations (2.1.13), (2.1.15) and
(2.1.16) will form the basis for the model equations to be
used in the present investigation.

It should be pointed out that for (b) and (c) to be
true when hydrostatic conditions are assumed, the kinetic
energy contained in the vertical component of the motion
cannot be included in the overall total kinetic energy.
However, it can be said that the amount neglected is an
insignificant fraction of the total energy involved in
synoptic and larger scale systems and, therefore, the
omission is normally of small consequence.

2.2 Sensible Heating and Static Stability

In order to incorporate sensible heat exchange in the
modelling the First Law of thermodynamics will be used in
the form

$$c_p T \frac{d \ln \theta}{dt} = \dot{H} \tag{2.2.1}$$

where $\dot{H}$ is the rate at which external heat is added per unit
mass (i.e. $\dot{H} = dH/dt$). By applying (2.1.7) the First Law
states that the total rate of change of potential
temperature is

$$\frac{d\theta}{dt} = \left(\frac{p}{100}\right)^{-\kappa} \frac{\dot{H}}{c_p} \tag{2.2.2}$$

This is simply the diabatic form of (2.1.13).

The rate and direction of sensible heat flow across the interface of any two adjacent environments is largely dictated by the local difference in the respective temperatures on either side. In the atmospheric situation, where the air is in motion over a comparatively fixed underlying surface, the speed and turbulent state of the overriding air flow are also of primary import in determining a heat exchange rate. An estimate of the turbulent exchange of sensible heat at the earth's surface can be made using

$$\dot{H}_s = C V_s \left(T_g - T_a \right) \qquad (2.2.3)$$

where T is the surface air temperature, T the underlying ground or sea temperature and V_s the surface wind speed. The term C is determined from atmospheric parameters (such as the surface drag coefficient) and is constant for a given value of V_s. Equation (2.2.3) is discussed in detail by Budyko (1956) and generally has been applied to calculations of turbulent heat transfers over water surfaces rather than over the continents. Haltiner (1967) has used this form of surface heat input in his model. As a further approximation, however, Haltiner (1967) assumed that the heating was distributed through the atmosphere according to a vertical profile of

$$\dot{H}(p) = \dot{H}\left(\frac{p}{p_s}\right)^r \qquad (2.2.4)$$

for which $\dot{H}(p)$ represents the rate of sensible heating

occurring at pressure p, p_s is surface pressure and r is a constant taken to equal 2 for his investigation.

In the present study no assumptions will be made as to a predetermined vertical distribution for sensible heating. Rather, considerations of the turbulent nature of the atmosphere will be used to provide a mechanism for vertically transporting heat. The process of heat transport by turbulent eddies in the air is known as thermal turbulent diffusion. If $\dot{H}_j$ denotes the sensible heating rate at some level j in the modelled atmosphere then it can be separated into two parts

$$\dot{H}_j = R_j + S_j \qquad (2.2.5)$$

where R and S are the vertical and horizontal turbulent thermal diffusion terms, respectively.

The vertical diffusion of sensible heat will be defined by

$$R_j = g \frac{\partial h_j}{\partial p} \qquad (2.2.6)$$

in which g is the gravitational acceleration. Here h_j represents the vertical heat flux given by

$$h_j = \rho^2 g \, c_p \, K_v \left[\left(\frac{\partial \theta_j}{\partial p} \right) - \Gamma \right] \qquad (2.2.7)$$

where K_v is the vertical kinematic eddy diffusivity coefficient and Γ (°C/kPa) acts as a measure of the countergradient. The concept of an atmospheric countergradient flux is used to explain observations of the

occurrence of some upward heat flux even under slightly stable conditions. The lateral diffusion term is to be determined by

$$S_j = c_p K_H \nabla^2 T_j = c_p K_H \left(\frac{P_j}{100}\right)^\kappa \nabla^2 \theta \qquad (2.2.8)$$

where K_H is the horizontal kinematic eddy diffusivity coefficient.

To establish a two-level model which contains a self-determining variable static stability the thermodynamic and vorticity equations are to be applied at the same information levels, as opposed to the normal situation when the thermodynamic equation is used at one level only. Figure 2.1 shows the vertical structure of a two-level model where the isobaric surfaces 1, 2 and 3 represent the primary information levels. Therefore, with the thermodynamic equation employed at levels 1 and 3, a measure of the variable static stability at level 2 can be obtained by a vertical finite-difference representation of $\partial\theta/\partial p$ in the form

$$\left(\frac{\partial \theta_2}{\partial p}\right) \simeq \frac{\theta_3 - \theta_1}{P_3 - P_1} = 2 \frac{\theta_3 - \theta_1}{P_3 - P_1} \qquad (2.2.9)$$

From (2.2.7) it is clear that the transport of sensible heat in the vertical is a direct function of stability. Increased atmospheric instability ($\partial\theta/\partial p > \Gamma$) implies greater upward heat flow while conditions of strong stability ($\partial\theta/\partial p < \Gamma$) will create downward heat flux. In the ordinary quasi-geostrophic two-level model with the static stability

$\omega = 0$ LEVEL 0

P_0

$P_3 = \dfrac{P_0 - P_4}{4}$ ——— ψ_1 ——— X_1 ——— θ_1 ——— 1

$P_2 = \dfrac{P_0 - P_4}{2}$ —— $\psi_2 = \dfrac{\psi_1 + \psi_3}{2}$ ——— $\theta_2 = \dfrac{\theta_1 + \theta_3}{2}$ —— 2

$P_1 = \dfrac{3(P_0 - P_4)}{4}$ ——— ψ_3 ——— X_3 ——— θ_3 ——— 3

$\omega = 0$ LEVEL 4

P_4
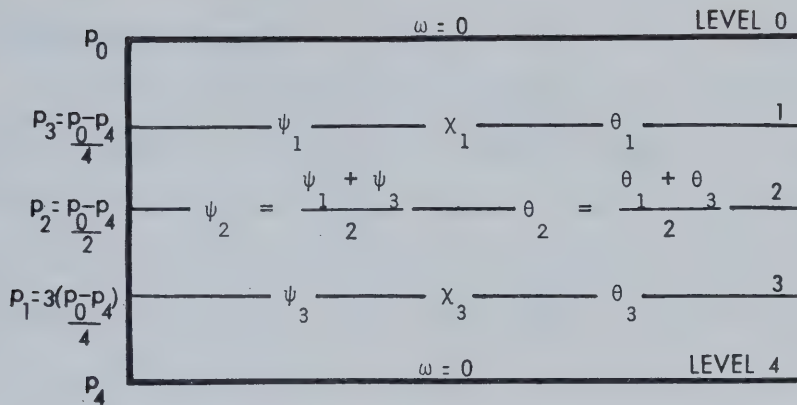
Fig. 2.1. Vertical structure of the Lorenz (1960) two-level model
of the atmosphere showing the isobaric information levels. A
measure of the atmospheric static stability is given by

$(\theta_3 - \theta_1)/(p_3 - p_1).$

constant it is not possible to include the effect of a
variable rate of vertical heat transport. As a result
diabatic heating in such models is normally input at level 2
(Figure 2.1) as a mean rate for the entire column of air
extending from the surface to the top of the atmosphere.
Since the whole atmosphere is essentially treated as one
layer for heat input purposes the vertical diffusion terms
can be ignored. Haltiner's (1967) vertical profile as given
by (2.2.4) also precludes the need for vertical diffusion
terms, although the profile is very dependent on the choice

of a value for the constant r which has no physical interpretation.

2.3 Frictional Terms

In Chapter 1 reference was made to two studies which reported investigations of the dynamic response changes created by inserting friction into a quasi-geostrophic two-level model. However, as used by Holopainen (1961), and Haltiner and Calverly (1965), the model embodied only surface-based frictional effects. In the current investigation those frictional effects created by small-scale turbulent eddies in the atmospheric flow well removed from the earth's surface will also be considered.

The governing vorticity equation for the present model will be of a form similar to (2.1.14) except that a non-zero term will be inserted to account for frictional influences. Since it appears by way of the vorticity equation this frictional term will be treated as a rate of vorticity change caused by eddy momentum diffusion. If the term F_j represents the effect of friction in the model at an isobaric level j then, as with the approach employed for the sensible heating, it can be separated into two parts

$$F_j = N_j + M_j \qquad (2.3.1)$$

in which N and M are the turbulent diffusion terms representing the vertical and horizontal frictional effects, respectively.

By analogy with the thermal diffusion term R, the frictional effect due to vertical momentum diffusion will be given by

$$N_j = -g \frac{\partial \tau_j}{\partial p} \qquad (2.3.2)$$

where τ_j represents the curl of the frictional stress acting on a horizontal surface and is defined as

$$\tau_j = \vec{\nabla} \times \rho K_H \left(\frac{\partial \vec{V}}{\partial z} \right)_j = -\rho^2 g K_H \frac{\partial}{\partial p} \nabla^2 \psi_j \qquad (2.3.3)$$

for which K_H is the vertical kinematic coefficient of eddy viscosity. Similarly, following closely the form given for the heating term S, the horizontal momentum diffusion term will be written as

$$M_j = \vec{\nabla} \times \left(K_M \nabla^2 V_j \right) = K_M \nabla^2 \left(\nabla^2 \psi_j \right) \qquad (2.3.4)$$

in which K_M is the horizontal kinematic coefficient of eddy viscosity.

2.4 The Model Equations

Following the vertical structure as given in Figure 2.1 the surface pressure value at the bottom of the current model is taken to be 100 kPa. The uppermost level is then given a pressure of 20 kPa as a representative value of the top of the troposphere. A common alternative is to let the upper level of the model correspond to the top of the entire atmosphere (p=0). However, for this study it will be assumed that the tropopause acts as a lid on the

tropospheric motions. The remaining information levels in the model are arranged such that each is separated by a 20 kPa layer. Thus levels 1, 2 and 3 correspond to the 40, 60 and 80 kPa pressure surfaces, respectively.

The governing equations as applied at the different levels in the modelled troposphere are

$$\nabla^2\left(\frac{\partial\phi_2}{\partial p}\right) - \vec{\nabla}f\cdot\nabla\left(\frac{\partial\psi_2}{\partial p}\right) - f\nabla^2\left(\frac{\partial\psi_2}{\partial p}\right) = 0 \qquad (2.4.1)$$

$$\frac{\partial\theta_j}{\partial t} + J(\psi,\theta) + \vec{\nabla}\chi\cdot\vec{\nabla}\theta_j + \omega_j\left(\frac{\partial\theta_j}{\partial p}\right) = \left(\frac{p_j}{100}\right)^{-\chi}\frac{\dot{H}_j}{c_p} \qquad (2.4.2)$$

$$\frac{\partial\psi_j}{\partial t} + J(\psi_j, \nabla^2\psi_j + f) + \vec{\nabla}\chi_j\cdot\vec{\nabla}f - f\left(\frac{\partial\omega_j}{\partial p}\right) = F_j \qquad (2.4.3)$$

where j=1 or 3. Equation (2.1.15) has been differentiated with respect to pressure and applied at level 2 to form (2.4.1). The diabatic thermodynamic equation and vorticity equation (friction included) as employed at levels 1 and 3 are given by (2.4.2) and (2.4.3). The compatible form of the continuity equation remains as (2.1.12) with (2.1.11) an inherent assumption.

The equation of state for an ideal gas will also be used in the form

$$p = \rho RT \qquad (2.4.4)$$

and (2.1.7) is understood to be an additional equation of state applicable to the model.

The purpose of differentiating the linear balance

equation with respect to pressure is to derive a formulation
which does not contain geopotential as a variable in the
model.   Replacement of $\partial\phi/\partial p$ using (2.1.11) and the
subsequent use of (2.4.4) and (2.1.7) allows (2.4.1) to be
rewritten as

$$\frac{R\rho^{\kappa-1}}{100^\kappa} \; \vec{\nabla}^2\theta_2 = \vec{\nabla}f\cdot\left(\vec{\nabla}\frac{\partial\psi_2}{\partial p}\right) + f\,\vec{\nabla}\left(\vec{\nabla}\frac{\partial\psi_2}{\partial p}\right) \qquad (2.4.5)$$

The term $\vec{\nabla}\partial\psi/\partial p$ represents the change of the rotational
component of the wind with changing pressure and can be
thought of as a form of vertical shear.   Therefore (2.4.5)
is a form of thermal wind relation for the mid-troposphere.

CHAPTER 3

NUMERICAL PROCEDURE

3.1 Boundary Conditions and Coefficient Values

If the earth's surface is assumed horizontal and the
lowest level of the model remains fixed on the ground the
proper lower boundary conditions are z=0 and w=dz/dt=0,
where z is height. However, for convenience the conditions
at the bottom of the present model will be taken to be

$$\omega = 0 \text{ and } p=p_4 = 100 \text{ kPa} \qquad (3.1.1)$$

These conditions state that the pressure at the bottom of
the model remains fixed, but they do not imply a constant
height field because z is not necessarily constant at the
lower boundary. As will be discussed in detail later in
this chapter, level 4 of the model is not always found at
the sea surface. However, the variation of sea-level
pressure from 100 kPa will be a perturbation quantity.
Therefore, the lower boundary of the model will be treated
as if it remained within a surface-based layer where the
eddy stress term and the vertical heat flux are constant.
No orographic variations are included in the lower boundary
conditions.

At the top of the model the condition that the

27

tropopause acts as a lid on tropospheric motions gives

$$\omega = 0 \quad \text{at} \quad p = p_o = 20 \text{ kPa} \tag{3.1.2}$$

To prevent the diffusion of heat and momentum across the tropopause the upper boundary conditions will also necessarily include

$$h = 0 \text{ and } \tau = 0 \text{ at } p = 20 \text{ kPa} \tag{3.1.3}$$

By adopting these boundary conditions it is possible to expand the friction and heating terms more explicitly. The expression for the vertical diffusion of sensible heat (2.1.6) is evaluated at level 1 using vertical finite-differencing to give

$$R_1 = -g \frac{h_o - h_2}{\Delta p} = g \frac{h_2}{\Delta p} \tag{3.1.4}$$

where p represents a 40 kPa interval and h_o is the vertical heat flux at p=0 which by (3.1.3) is zero. Using (2.2.7) to replace h_2 (3.1.4) becomes

$$R_1 = \rho^2 g^2 c_p \frac{K_v}{\Delta p} \left(\frac{\theta_3 - \theta_1}{\Delta p} - \Gamma \right) = k_h c_p \left(\theta_3 - \theta_1 - \Delta p \Gamma \right) \tag{3.1.5}$$

The coefficient $k_h = \rho^2 g^2 K_v / \Delta p^2$ has been introduced into (3.1.5) for simplification. The same procedure can be applied at level 3 so that

$$R_3 = -g \frac{h_2 - h_4}{\Delta p} \tag{3.1.6}$$

where the term h_2 is to be replaced as was done in (3.1.5). At the lower boundary of the model a constant surface heat

flux layer has been assumed. Surface heat flux will now be defined to be

$$h_s = h_4 = \rho C_D c_p \left(T_g - T_a \right) V_s \qquad (3.1.7)$$

for which C_D is the surface drag coefficient. To convert (3.1.7) to a heating rate per unit mass in a form similar to that of (2.2.3) a constant C is introduced, where

$$C = \frac{g \rho c_p C_D}{\Delta p} \qquad (3.1.8)$$

The resulting expression for R_3 is, therefore

$$R_3 = -k_h c_p \left(\theta_3 - \theta_1 - \Delta p \, \Gamma \right) + C V_s \left(T_g - T_a \right) \qquad (3.1.9)$$

The entire approach as outlined above can be applied in a similar way to the vertical momentum diffusion terms. At level 1 the expression for the friction term in the vertical using (2.3.2) and (2.3.3) is

$$N_1 = g \frac{\tau_0 - \tau_2}{\Delta p} = -k_i \nabla^2 \left(\psi_1 - \psi_3 \right) \qquad (3.1.10)$$

where the coefficient $k_i = \rho^2 g^2 K_N / \Delta p^2$ is analogous to k_h. At the lower boundary the constant stress term is defined to be

$$\tau_4 = \frac{\Delta p k_s}{g} \nabla^2 \psi_4 \qquad (3.1.11)$$

for which k_s is a constant. The term N_3 is found to be

$$N_3 = g \frac{\tau_2 - \tau_4}{\Delta p} = k_i \nabla^2 \left(\psi_1 - \psi_3 \right) - k_s \nabla^2 \psi_4 \qquad (3.1.12)$$

It now remains to assign numerical values to the coefficients k_h, k_i and k_s. For the purpose of estimating

these values it will be convenient to assume $K_V = K_N$ and
therefore $k_i = k_h$. In unstable cases there is some basis for
the argument that the magnitude of K_V is greater than K_N
(Lumley and Panofsky,1964; Businger,1973). However, over a
large range of stability conditions K_V and K_N have been
found to be of similar magnitude. As well, the value chosen
for K_V (K_N) in this study will be indicative of near-neutral
stability conditions rather than of the unstable regime.
Using $\partial \bar{\theta}/\partial p \simeq \Gamma$ and values suggested by Deardorff (1967) K_V is
taken as being 6×10^1 m²/s. A representative 60 kPa winter
temperature value at mid-latitudes would be between -18°C
and -25°C based on mean January temperature data
(Gates,1975). Applying (2.1.7) to determine density,
possible values for k_i and k_h are then 0.9×10^{-6} to 1.1×10^{-6}
s⁻¹. Estimates of k_i as used in other two-level models
range from 0.5×10^{-6} s⁻¹ (Charney,1959; Kikuchi,1969) to 10^{-6}
s⁻¹ (Egger,1976). For this investigation $k_i = k_h = 10^{-6}$ s⁻¹ is
used in all numerical computations.

The most commonly used value for the coefficient k_s is
4×10^{-6} s⁻¹ as employed by Phillips (1956) and Charney
(1959). Derome and Wiin-Nielson (1971) have experimented
with a surface friction coefficient which was altered
between 4×10^{-6} and 6×10^{-6} s⁻¹. The effect of increasing the
surface friction coefficient on the behavior of their quasi-
geostrophic steady-state model was relatively small. These
investigators also studied the effect of having one constant
surface friction coefficient over the land and a smaller

constant value over the oceans. The consequence on the
model predictions was only of serious import when the ratio
of the two coefficients had reached a value of 6 or more.
At a ratio of 2 little difference was observed over assuming
one uniform friction coefficient. The earth's surface will
be considered to be uniform for the purposes of this study
and the imposed surface friction coefficient will be taken
to be 4×10^{-6} s^{-1} in most calculations.

Other coefficients to be assigned numerical values are
K_M and K_H. Once more, for simplification, it is presupposed
that $K_M = K_H$. In assuming Fickian diffusion for the
dispersion of clouds and inert tracers in the lower
atmosphere, the observational evidence as suggested by Hage
(1964) and Bauer (1974) would indicate that the order of
magnitude of the horizontal diffusivity coefficient is 10^5-
10^6 m^2/s for large-scale diffusion processes (i.e. those
with a travel time of more than few days and an eddy space
scale of greater than few hundred meters). Although the
data refer to the horizontal dispersion of mass and may not
be totally indicative of linear momentum or heat dispersion,
they do provide a useful quantitative estimate of the order
of magnitude which should be looked at. Phillips (1956) has
employed a value of $K_M = 10^5$ m^2/s in his modelling as does
Kikuchi (1969). The value fixed for K_M and K_H in this study
is also 10^5 m^2/s.

Surface sensible heating, as was indicated earlier, is
dependent on the product of the constant C and the mean

surface wind speed V_s. In order to assign a numerical value
to C it is first necessary to make an estimate of the
surface drag coefficient C_D. Cressman (1960) has devised a
general scheme for calculating surface drag coefficients.
The coefficients are evaluated using two components, the
first being a dimensionless constant of 1.296×10^{-3} for all
surfaces and the second is an additive quantity which is a
function of the terrain roughness. Over water surfaces the
total drag coefficient is resolved to be $\leq 1.3 \times 10^{-3}$ while
over land surfaces the variation in C_D values is 1.3×10^{-3} to
8.0×10^{-3}, with the larger end of this scale reflecting very
mountainous terrain. If it is assumed that $C_D = 1.3 \times 10^{-3}$ for
a surface wind of $V_s = 10$ m/s (i.e. measured at anemometer
height) then a numerical estimate of C as calculated from
(3.1.8) would be 8×10^{-3} to 9×10^{-3} J/(kg m °C). The product
CV_s then compares favourably with the value of 10^{-2} J/(kg s
°C) used by Haltiner (1967) to represent the same quantity.
As a matter of procedure the rate of sensible heat input
will be varied when analyzing the model's dynamic stability
characteristics. The heating rates used will remain within
a range of 0 to 2×10^{-2} J/(kg s °C).

3.2 Perturbation Equations

A useful technique for representing conditions in the
mid-troposphere is to create new variables which describe
the vertical mean and differential quantities across levels
1 and 3 of the model. For example, if b is any scalar

quantity then the averaged or mean value of b for the layer
between the two levels is given by $(b_1+b_3)/2$. Similarly the
differential value would be $(b_1-b_3)/2$. If this method is
applied to (2.4.2) and (2.4.3) the equations take the
following forms

$$\frac{\partial \theta}{\partial t} + J\left(\psi,\theta\right) + J\left(\eta,\sigma\right) + \vec{\nabla}\chi \cdot \vec{\nabla}\sigma - \frac{\omega_2 \sigma}{\Delta p} = \left(\frac{2}{5}\right)^{-\varkappa}\frac{H_1}{2c_p} + \left(\frac{4}{5}\right)^{-\varkappa}\frac{H_3}{2c_p} \qquad (3.2.1)$$

$$\frac{\partial \sigma}{\partial t} + J\left(\psi,\sigma\right) + J\left(\eta,\theta\right) + \vec{\nabla}\chi \cdot \vec{\nabla}\theta = \left(\frac{2}{5}\right)^{-\varkappa}\frac{H_1}{2c_p} - \left(\frac{4}{5}\right)^{-\varkappa}\frac{H_3}{2c_p} \qquad (3.2.2)$$

$$\frac{\partial^2 \psi}{\partial t} + J\left(\psi, \nabla^2 \psi + f\right) + J\left(\eta, \nabla^2_\eta\right) = \frac{F_1+F_3}{2} \qquad (3.2.3)$$

$$\frac{\partial \nabla^2_\eta}{\partial t} + J\left(\eta, \nabla^2 \psi + f\right) + J\left(\psi, \nabla^2_\eta\right) + \vec{\nabla}\chi \cdot \vec{\nabla}f - \frac{f\omega_2}{\Delta p} = \frac{F_1-F_3}{2} \qquad (3.2.4)$$

Equations (3.2.1) and (3.2.3) now represent the averaged
thermodynamic and vorticity equations, respectively, while
(3.2.2) and (3.2.4) are their difference counterparts. The
variables as they now occur are $\psi = (\psi_1 + \psi_3)/2$, $\eta = (\psi_1 - \psi_3)/2$,
$\theta = (\theta_1 + \theta_3)/2$, $\sigma = (\theta_1 - \theta_3)/2$ and $\chi = (\chi_1 - \chi_3)/2$. Vertical finite-
differencing has been used for those terms involving $(\partial/\partial p)$
and it has been assumed that at any given time σ is
representative of the static stability over the entire
troposphere $(\theta_j = \theta_{j+1} + \sigma)$.

    With the approximation that $\theta_2 = (\theta_1 + \theta_3)/2$ (2.4.5) as
applied at level 2 becomes

$$R \frac{3}{5}\varkappa^{\varkappa-1} \nabla^2 \theta - \vec{\nabla}\left(f \vec{\nabla}\eta\right) = 0 \qquad (3.2.5)$$

while the continuity equation for the model using the upper
and lower boundary conditions on ω_2 can be expressed as

$$\frac{1}{2}\left[\left(\frac{\partial \omega_2}{\partial p}\right)-\left(\frac{\partial \omega_3}{\partial p}\right)\right] = \frac{\omega_2}{\Delta p} = -\nabla^2 \chi \qquad (3.2.6)$$

In order to analyze the dynamics of this system a
perturbation approach is used to linearize the equations.
The perturbation method assumes that atmospheric motion
consists of small fluctuations superimposed on a basic or
steady-state flow. The fundamental premises are (Haltiner
and Martin, 1957):

    (a) the steady-state motion satisfies the
        governing equations;

    (b) the overall motion (steady-state plus
        perturbation) also satisfies the equations;
        and

    (c) squares (or higher orders) and products of
        perturbation variables appearing in the
        equations may be neglected in comparision with
        first crder terms.

For instance

$$\psi = \bar{\psi} + \psi' \qquad (3.2.7)$$

where ψ denotes the total value of the quantity, $\bar{\psi}$ is the
steady-state value and ψ' refers to the perturbation value.
The same representation can be applied to η, θ, σ and χ.

The steady-state flow as is suggested by its name is
not a function of time. Further, it will be assumed that
such flow is zonal and non-divergent in behavior. Thus,
both $\bar{\chi}$ and $\bar{\omega}$ are necessarily zero. The basic state terms $\bar{\psi}$,

$\bar{\theta}$, $\bar{\eta}$ and $\bar{\sigma}$ are to be regarded as linear functions of y alone while the perturbations are to be treated as simple functions of x, y and t.

For sensible heat exchange the earth's surface is regarded as an infinite heat source (or sink) implying that its temperature field remains constant and that T_a tends to adopt to T_g. Therefore, under steady-state conditions the surface air can be assumed to be in thermal equilibrium with the underlying surface. As a result $\bar{T}_a = T_g$ and the heating rate is dependent on surface air temperature fluctuations according to

$$CV_s\left(T_g - T_a\right) = k_t\left(-T_2'\right) \qquad (3.2.8)$$

Variations in V_s may be neglected since T_a' is already a perturbation quantity and so $k_t = C\bar{V}_s$.

If the potential temperature at the lower boundary of the model is linearly extrapolated from the 60 kPa level as $\theta_4 = \theta - 2\sigma$, then by assuming a sea-level pressure of 100 kPa the atmosphere-ground temperature difference is $T_a' = \theta_4' = \theta' - 2\sigma'$. This assumption is not totally valid, however, and a correction term is required to describe the possible variations in the sea-level pressure from 100 kPa.

An estimate of the pressure deviations at z=0 can be obtained by using the general form of (2.4.1) and substituting for the geopotential with $\phi = gz$. For a first approximation the term $\vec{\nabla}f \cdot \vec{\nabla}\left(\partial\psi/\partial p\right)$ is neglected and the remaining partial derivatives are replaced by finite

numerical estimates giving

$$\frac{\delta z}{\delta p} \approx \frac{f}{g} \frac{\delta \psi}{\delta p} \tag{3.2.9}$$

where δz and $\delta \psi$ represent changes in the height and streamfunction values over some very small pressure interval δp. Perturbations in the lower boundary boundary stream function values are given by $\psi_4' = \psi' - 2\eta$. Hence, assuming $\delta \psi = \psi_4'$ and using (3.2.10) the variation in the 100 kPa level height is $\delta z = f(\psi' - 2\eta')/g$. Moreover, from the hydrostatic assumption (2.1.11), the change in pressure in going from 100 kPa to sea-level pressure is $\delta p = -\rho f(\psi' - 2\eta')$. Figure 3.1 illustrates a situation where $\psi' - 2\eta > 0$ and the sea-level pressure is greater than 100 kPa.

From (2.1.7), (2.1.11) and (2.4.4) it is possible to derive the following expression for the atmospheric lapse rate

$$\frac{\partial T}{\partial z} = \left(\frac{\partial \theta}{\partial p} \frac{\partial p}{\partial z} \right) \left(\frac{P}{100} \right)^x - \gamma_d \tag{3.2.10}$$

in which $\gamma_d = g/c_p$ is the dry adiabatic lapse rate. Replacing the partial derivative $\partial T/\partial z$ with its finite representation $\delta T/\delta z$ and using $\partial \theta/\partial p = -2\sigma/\Delta p$ for the modelled stability parameter gives

$$\delta T = -\delta z \left[\gamma_d - \frac{2\rho g \sigma}{\Delta p} \left(\frac{P}{100} \right)^x \right] \tag{3.2.11}$$

where δT is now the temperature decrease in going from $z = 0$ to the height of the model's lower boundary δz. The total variation in the surface temperature is

$\theta - \sigma$ $\qquad$ $\psi - \eta$ $\qquad$ LEVEL 3

$\theta_4 = \theta - 2\sigma$ $\qquad$ $\psi_4 = \psi - 2\eta$ $\qquad$ LEVEL 4

$$\delta z = \frac{f}{g}(\psi - 2\eta) > 0$$
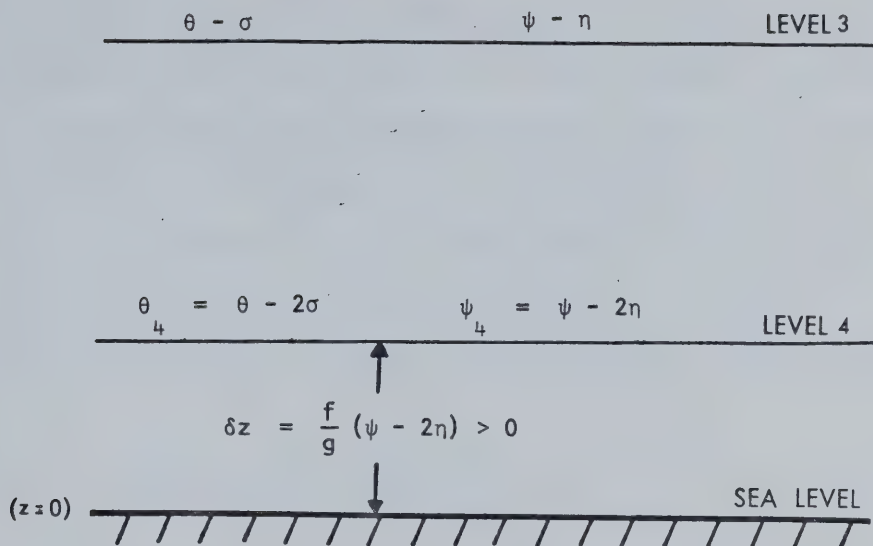
$(z = 0)$ $\qquad$ SEA LEVEL

Fig. 3.1. Deviation of the sea-level pressure field from 100 kPa. Sea-level pressure values are estimated using 100 - δp (kPa), where $\delta p = - \rho g \delta z = - \rho f(\psi - 2\eta)$. The vertical cross-section shown displays a situation where the 100 kPa level is found above sea surface.

$$T_a' = \theta_4' - \delta T = \left(\theta' - 2\sigma'\right) + \frac{f}{g}\left(\psi' - 2\eta'\right)\left[\gamma_d - \frac{2\rho g\bar{\sigma}}{\Delta p}\left(\frac{100 - \delta p}{100}\right)^{\kappa}\right] \qquad (3.2.12)$$

To a very good approximation $((100 - \delta p)^{\kappa}/100) \simeq 1$ and as a result may be dropped from (3.2.13). The total surface heating rate then takes the perturbation form

$$-k_s T_a' = k_s\left[2\sigma' - \theta' - \frac{f}{g}\left(\psi' - 2\eta'\right)\left(\gamma_d - \frac{2\rho g\bar{\sigma}}{\Delta p}\right)\right] \qquad (3.2.13)$$

In addition to having no surface heating under steady-state conditions, it will also be presupposed that there is

no sensible heating from diffusion in the basic flow. This
has already been accomplished for the horizontal diffusion
term by assuming that the steady-state quantities are linear
on the y-axis and constant along the x-axis. In the
vertical diffusion term it is achieved by setting the
countergradient $\partial\bar\theta/\partial p$ equal to $-2\bar\sigma/\triangle p$ in the model.
Vertical diffusion at level 1 as expressed in (3.1.5) is
then

$$R_1 = k_h c_p \left[-2\sigma - \frac{-2\bar\sigma}{\triangle p}\, \triangle p \right] = -2 k_h c_p \sigma' \qquad (3.2.14)$$

A similar substitution can be made in (3.1.9). The value of
$\bar\sigma$ used for the modelled atmosphere is based on January
average temperature fields at 40 kPa and 80 kPa for the
Northern Hemisphere (Gates,(1975)). Over the hemisphere
and, in particular, over the North Pacific the mean value of
the static stability is approximately 22 to 23°C for the 40
kPa layer. This would give a countergradient $\partial\bar\theta/\partial z$ of 4 to
5°C/km. Typically, estimates of Γ in the atmosphere vary
from 0.65°C/km under clear skies to roughly 5°C/km under
cloudy conditions (Deardorff,1967).

    The linearized versions of (3.2.1)-(3.2.5), after
substituting for ω_2 using (3.2.6), take the form

$$\frac{\partial\theta'}{\partial t} + \frac{\partial\psi'}{\partial x}\frac{\partial\bar\theta}{\partial y} + U\frac{\partial\theta'}{\partial x} + \frac{\partial\eta'}{\partial x}\frac{\partial\bar\sigma}{\partial y} + U_T\frac{\partial\sigma'}{\partial x} + \frac{\partial\chi'}{\partial y}\frac{\partial\bar\sigma}{\partial y} + \bar\sigma\left(\frac{\partial^2\chi'}{\partial x^2}+\frac{\partial^2\chi'}{\partial y^2}\right)$$

$$= K_H\left(\frac{\partial^2\theta'}{\partial x^2}+\frac{\partial^2\theta'}{\partial y^2}\right) + a_2 k_h \sigma'$$

$$+ \frac{a_3 k_c}{c_p}\left[2\sigma' - \theta' - \frac{f}{g}(\psi' - 2\eta')\left(\gamma_d - \frac{2\rho g\bar\sigma}{\triangle p}\right) \right] \qquad (3.2.15)$$

$$\frac{\partial \sigma'}{\partial t} + \frac{\partial \psi'}{\partial x}\frac{\partial \bar{\sigma}}{\partial y} + U\frac{\partial \sigma'}{\partial x} + \frac{\partial \eta'}{\partial x}\frac{\partial \bar{\theta}}{\partial y} + U_T\frac{\partial \theta'}{\partial x} + \frac{\partial \chi'}{\partial y}\frac{\partial \bar{\theta}}{\partial y}$$

$$= K_H \left(\frac{\partial^2 \sigma'}{\partial x^2} + \frac{\partial^2 \sigma'}{\partial y^2}\right) - a_1 k_h \sigma'$$

$$- \frac{a_3 k_t}{c_p}\left[2\sigma' - \theta' - \frac{f}{g}\left(\psi' - 2\eta'\right)\frac{\delta_d - 2\rho g\bar{\sigma}}{\Delta p}\right] \tag{3.2.16}$$

$$\frac{\partial}{\partial t}\left(\frac{\partial^2}{\partial x^2} + \frac{\partial^2}{\partial y^2}\right)\psi' + \frac{\partial \psi'}{\partial x}\frac{\partial f}{\partial y} + U\frac{\partial^3 \psi'}{\partial x^3} + U\frac{\partial^3 \psi'}{\partial x \partial y} + U_T\frac{\partial^3 \eta'}{\partial x^3} + U_T\frac{\partial^3 \eta'}{\partial x \partial y^2}$$

$$= -\frac{k_s}{2}\left(\frac{\partial^2}{\partial x^2} + \frac{\partial^2}{\partial y^2}\right)\left(\psi' - 2\eta'\right) + K_M\left(\frac{\partial^4}{\partial x^4} + \frac{\partial^4}{\partial y^4}\right)\psi' \tag{3.2.17}$$

$$\frac{\partial}{\partial t}\left(\frac{\partial^2}{\partial x^2} + \frac{\partial^2}{\partial y^2}\right)\eta' + \frac{\partial \eta'}{\partial x}\frac{\partial f}{\partial y} + U_T\frac{\partial^3 \psi'}{\partial x^3} + U_T\frac{\partial^3 \psi'}{\partial x \partial y} + U\frac{\partial^3 \eta'}{\partial x^2}$$

$$+ U\frac{\partial^3 \eta'}{\partial x \partial y^2} + f\left(\frac{\partial^2}{\partial x^2} + \frac{\partial^2}{\partial y^2}\right)\chi' = \frac{k_s}{2}\left(\frac{\partial^2}{\partial x^2} + \frac{\partial^2}{\partial y^2}\right)\left(\psi' - 2\eta'\right)$$

$$- 2k_i\left(\frac{\partial^2}{\partial x^2} + \frac{\partial^2}{\partial y^2}\right)\eta' + K_M\left(\frac{\partial^4}{\partial x^4} + \frac{\partial^4}{\partial y^4}\right)\eta' \tag{3.2.18}$$

$$\frac{3^{k-1}}{5^k} R\left(\frac{\partial^2}{\partial x^2} + \frac{\partial^2}{\partial y^2}\right)\theta' = \left(\frac{\partial^2}{\partial x^2} + \frac{\partial^2}{\partial y^2}\right)\eta' \tag{3.2.19}$$

where $U = -\partial\bar{\psi}/\partial y$ represents the mean zonal wind and $U_T = -\partial\bar{\eta}/\partial y$ is the vertical wind shear of the basic state. The coefficients a_i ($i=1,2,3$) are; $a_1 = (2/5)-k+ (4/5)-k = 2.635$, $a_2 = (4/5)-k - (3/5)-k = -0.233$ and $a_3 = (4/5)-k/2 = 0.533$.

3.3 Stability Analysis

In order to investigate the stability of those perturbations in the baroclinic atmosphere depicted by the

model, harmonic-wave solutions of the following form are assumed

$$\psi' = \hat{\psi}(y)\exp\left[im(x-ct)\right] \qquad \eta' = \hat{\eta}(y)\exp\left[im(x-ct)\right]$$

$$\theta' = \hat{\theta}(y)\exp\left[im(x-ct)\right] \qquad \sigma' = \hat{\sigma}(y)\exp\left[im(x-ct)\right] \qquad (3.3.1)$$

$$\chi' = \hat{\chi}(y)\exp\left[im(x-ct)\right]$$

where $m=2\pi/L_y$ is the wavenumber and L_x is the wavelength on the x-axis, c is the phase velocity of the wave, $\sqrt{i} = -1$, and $\hat{\psi}(y)$, $\hat{\eta}(y)$, $\hat{\theta}(y)$, $\hat{\sigma}(y)$ and $\hat{\chi}(y)$ are the wave amplitudes. The latitudinal dependence of the perturbations enters through the amplitudes which will be given a simple meridional variation

$$\hat{\psi}(y) = \hat{\psi}\cos(ny) \qquad (3.3.2)$$

where $n=2\pi/L_y$ is the wavenumber and L_y is the wavelength in the y-direction. Substitution of these solutions into (3.2.16)-(3.2.20) leads to a set of homogeneous equations which can be represented in matrix form as

$$[B][A]=0 \qquad (3.3.3)$$

Here [A] is the amplitude matrix

$$\begin{Bmatrix} \hat{\psi} \\ \hat{\eta} \\ \hat{\theta} \\ \hat{\sigma} \\ \hat{\chi} \end{Bmatrix}$$

and [B] is the coefficient matrix defined as

$$
\begin{bmatrix}
(c-U)+b1 & b2 & 0 & 0 & 0 \\
b3 & (c-U)+b4 & 0 & 0 & b5 \\
b6 & b7 & -(c-U)+b8 & b9 & b10 \\
b11 & b12 & b13 & -(c-U)+b14 & b15 \\
0 & b16 & b17 & 0 & 0
\end{bmatrix}
$$

where

$b1 = \dfrac{\beta}{m^2+n^2} + \dfrac{ik_s}{2m} + \dfrac{iK_M\,(m^4+n^4)}{m\,(m^2+n^2)}$

$b2 = -\,U_T - \dfrac{ik_s}{m}$

$b3 = -\,U_T - \dfrac{ik_s}{2m}$

$b4 = \dfrac{\beta}{m^2+n^2} + \dfrac{i(k_s+2k_i)}{m} + \dfrac{iK_M\,(m^4+n^4)}{m\,(m^2+n^2)}$

$b5 = \dfrac{if}{m}$

$b6 = -\dfrac{5^{\varkappa}}{3^{\varkappa}}\dfrac{fU_T}{R} - \dfrac{ia_3k_t\,fG}{gc_pm}$

$b7 = \dfrac{5^{\varkappa}}{3^{\varkappa}}\,(1-\varkappa)\dfrac{fU_T}{R} + \dfrac{i2a_3k_t\,fG}{gc_pm}$

$b8 = \dfrac{i\,(m^2+n^2)\,K_H}{m} - \dfrac{ia_3k_t}{mc_p}$

$b9 = U_T + \dfrac{i2a_2k_t}{mc_p} + \dfrac{ia_3k_h}{m}$

$b10 = \dfrac{i5^{\varkappa}fU_Tn\tan(ny)}{3^{\varkappa}Rm} + \dfrac{i\,(m^2+n^2)\,\sigma_0}{m}$

$b11 = \dfrac{5^{\varkappa}(1-\varkappa)fU_T}{3^{\varkappa}R} + \dfrac{a_3k_t\,fG}{gc_pm}$

$b12 = -\dfrac{5^{\varkappa}fU_T}{3^{\varkappa-1}R} - \dfrac{i2a_3k_t\,fG}{gc_pm}$

$b13 = U_T + \dfrac{ia_3k_t}{mc_p}$

$b14 = -i\dfrac{(m^2+n^2)\,K_H}{m} - \dfrac{i2a_3k_t}{mc_p} - \dfrac{ia_2k_h}{m}$

$b15 = -\dfrac{i5^{\varkappa}fU_Tn}{3^{\varkappa-1}Rm}\,\tan(ny)$

$b16 = -\,f$

$$b_{17} = \frac{3^{\kappa-1}}{5^{\kappa}} \cdot R$$

In the coefficients $G = (\gamma_d - 2\rho g \bar{\sigma} / \Delta p)$ and $\beta = \partial f / \partial y$ is the meridional derivative of the Coriolis parameter. Use has also been made of the following relations

$$\frac{\partial \bar{\theta}}{\partial y} = \frac{-5^{\kappa} f U_T}{3^{\kappa-1} R} \tag{3.3.4}$$

$$\frac{\partial \bar{\sigma}}{\partial y} = (1-\kappa) \frac{5^{\kappa} f U_T}{3^{\kappa} R} \tag{3.3.5}$$

which were found by assuming a constant U_T in the mid-troposphere and then requiring the zonal flow to satisfy (3.2.20).

A necessary and sufficient condition that (3.3.3) has a non-trivial solution is that the determinant of [B] be zero. Expansion of the determinant and grouping of the terms in decreasing orders of (c-U) gives a cubic frequency equation which can be solved for a variety of wavenumbers, surface heating rates and steady-state quantities.

The phase velocities which are obtained in the solutions to this cubic frequency equation are typically complex values, $c = c_R + i c_I$, in which c_R represents the real portion and c_I the imaginary portion of the wave phase velocity. A perturbation wave is, therefore, of the form

$$\psi' = \hat{\psi} \cos(ny) \exp(m c_I t) \exp(im(x - c_R t)) \tag{3.3.6}$$

Such a waveform propagates in the west-east direction at a

speed c_R with a time-dependent numerical amplification (or damping) factor of $\exp(mc_I t)$. More specifically it is the value of c_I which determines the stability condition of the wave. The stability classifications are given in Table 1.

Table 1. Stability conditions for the harmonic wave-forms as a function of the imaginary portion of the phase velocity.

STABILITY CLASSIFICATION
UNSTABLE: c_I <0 , amplifying wave with time
NEUTRAL: c_I =0 , waveform unchanging
STABLE: c_I >0 , damped wave with time

The rate of amplification of an unstable wave is dependent on the exponent mc_I. A useful way of representing this growth rate is by a quantity known as the e-folding time (t_e) which is defined by

$$t_e = \frac{1}{mc_I} = \frac{L_x}{2\pi c_I} \qquad (3.3.7)$$

The value of t_e is the time required for an unstable wave to increase in amplitude by a factor of e=2.71828. The implication of a small e-folding time is that the waveform is very unstable and amplifying rapidly.

3.4 Wave Dynamics

When studying the phase and amplitude characteristics of the perturbations it is useful to express the harmonic solutions in a somewhat different form. Corresponding to each value of the phase velocity c_k (k=1,2,3) as given by the frequency equation, the system of equations represented by (3.3.3) can be solved for values of $\hat{\psi}_k$, $\hat{\eta}_k$, $\hat{\theta}_k$, $\hat{\sigma}_k$ and $\hat{\chi}_k$ if initial conditions for each perturbation wave are specified. The procedure is then to write the general perturbation waveforms as sums of components

$$\psi' = \sum_{k=1}^{3} \hat{\psi}_k \cos(ny) \exp im(x - c_k t)$$

$$\eta' = \sum_{k=1}^{3} \hat{\eta}_k \cos(ny) \exp im(x - c_k t)$$

$$\theta' = \sum_{k=1}^{3} \hat{\theta}_k \cos(ny) \exp im(x - c_k t)$$
$$\qquad (3.4.1)$$

$$\sigma' = \sum_{k=1}^{3} \hat{\sigma}_k \cos(ny) \exp im(x - c_k t)$$

$$\chi' = \sum_{k=1}^{3} \hat{\chi}_k \cos(ny) \exp im(x - c_k t)$$

It is convenient to substitute for the terms $\hat{\eta}_k$ and $\hat{\chi}_k$ from (3.3.3) using

$$\hat{\eta}_k = -\frac{b^{17}}{b^{16}} \hat{\theta}_k \qquad (3.4.2)$$

$$\hat{\chi}_k = -\frac{b^3}{b^5} \hat{\psi}_k + \left(\frac{c_k - U}{b^5} + b^4 \right) \frac{b^{17}}{b^{16}} \hat{\theta}_k \qquad (3.4.3)$$

The reduced system of equations in terms of $\hat{\psi}_k$, $\hat{\theta}_k$ and $\hat{\sigma}_k$ is

$$[D][E]=0 \tag{3.4.4}$$

where $[E]=\begin{pmatrix}\hat{\gamma}_k\\\hat{\theta}_k\\\hat{\sigma}_k\end{pmatrix}$, and $[D]=\begin{bmatrix}d^1_k & d^2_k & 0\\d^3_k & d^4_k & d^5_k\\d^6_k & d^7_k & d^8_k\end{bmatrix}$

The coefficients d^j_k (j=1,2,....,8 k=1,2,3) are

$$d^1_k = \left(c_k - U\right) + b^2 \qquad\qquad d^5_k = b^9$$

$$d^2_k = -\frac{b^2 b^{17}}{b^{16}} \qquad\qquad d^6_k = b^{11} - \frac{b^3 b^{15}}{b^5}$$

$$d^3_k = b^6 - \frac{b^3 b^{20}}{b^5} \qquad\qquad d^7_k = b^3 - \frac{b^{17}}{b^{16}}\left(b^{12} + b^{15}\left[\frac{c_k - U + b^{14}}{b^5}\right]\right)$$

$$d^4_k = \left(c_k - U\right) + b^8 - \frac{b^{17}}{b^{16}}\left[b^7 - b^{20}\frac{c_k - U + b^4}{b^5}\right] \qquad d^8_k = -\left(c_k - U\right) + b^{14}$$

The initial conditions specified at t=0 in the solutions to (3.4.4) are of the type

$$\gamma'(t=0) = \hat{\gamma}_o \, \cos(ny) \, \exp(imx)$$

$$\theta'(t=0) = \hat{\theta}_o \, \cos(ny) \, \exp(im\,x + \varepsilon_\theta) \tag{3.4.5}$$

$$\sigma'(t=0) = \hat{\sigma}_o \, \cos(ny) \, \exp(im\,x + \varepsilon_\sigma)$$

in which $\hat{\psi}_o$, $\hat{\theta}_o$ and $\hat{\sigma}_o$ are the initial amplitude values and ε_θ and ε_σ are the initial phase angles of θ' and σ' with respect to ψ'. For example, $\varepsilon_\theta < 0$ implies that the potential temperature wave initially lags the stream function, while $\varepsilon_\theta > 0$ means that the potential temperature wave leads. If $\varepsilon_\theta = 0$ the two waves are initially in phase.

It follows from (3.4.1) and (3.4.5) that

$$\sum_{k=1}^{3} \hat{\psi}_k = \hat{\psi}_o$$

$$\sum_{k=1}^{3} \hat{\theta}_k = \hat{\theta}_o \exp(i\varepsilon_\theta) \qquad (3.4.6)$$

$$\sum_{k=1}^{3} \hat{\sigma}_k = \hat{\sigma}_o \exp(i\varepsilon_\sigma)$$

Furthermore, from (3.4.4) $\hat{\theta}_k$ and $\hat{\sigma}_k$ can be expressed in terms of $\hat{\psi}_k$ as

$$\sum_{k=1}^{3} \hat{\theta}_k = \sum_{k=1}^{3} r_k \hat{\psi}_k$$

$$\sum_{k=1}^{3} \hat{\sigma}_k = \sum_{k=1}^{3} s_k \hat{\psi}_k \qquad (3.4.7)$$

where $r_k = -d^1_k / d^2_k$ and $s_k = -d^6_k / d^8_k + d^7_k d^1_k / (d^8_k d^2_k)$. From (3.4.6) and (3.4.7) the following general solutions for $\hat{\psi}_1$, $\hat{\psi}_2$ and $\hat{\psi}_3$ may be obtained

$$\hat{\psi}_1 = -\hat{\psi}_2 - \hat{\psi}_3 + \hat{\psi}_o$$

$$\hat{\psi}_2 = \frac{\hat{\sigma}_o e^{i\varepsilon_\sigma} - s_1 \hat{\psi}_o + (s_1 - s_3)\hat{\psi}_3}{s_2 - s_1} \qquad (3.4.8)$$

$$\hat{\psi}_3 = \frac{\hat{\theta}_o e^{i\varepsilon_\theta} + (r_1 - r_2)\left(\dfrac{\hat{\sigma}_o e^{i\varepsilon_\sigma} - s_1 \hat{\psi}_o}{s_2 - s_1}\right) - r_1 \hat{\psi}_o}{-(r_1 - r_2)\left(\dfrac{s_1 - s_3}{s_2 - s_1}\right) - r_2 + r_3}$$

Knowing the initial amplitude and phase values, the phase velocity c_k and parameters such as U, f, U_T, $\bar{\sigma}$ and others it is possible to determine $\hat{\psi}_3$ and then, in succession, the values of $\hat{\psi}_2$, $\hat{\psi}_1$, $\hat{\theta}_k$, $\hat{\sigma}_k$ and $\hat{\omega}_k$ with the component amplitudes for the vertical velocity determined from using the model's continuity equation and the velocity potential values $\hat{\chi}_k$. It is also useful to derive wave components representing surface sensible heating ($\hat{h}_k$) from the existing waveforms by employing (3.2.14).

Although each perturbation is written as a sum of three components, a single wave representation can be made which has its amplitude and phase angle as functions of time. From (3.4.1) and by writing the phase velocities and amplitudes in their complex form the mean perturbation stream function may be expressed as

$$\psi' = \sum_{k=1}^{3} \left(\hat{\psi}_{k_R} + i\hat{\psi}_{k_I} \right) \cos(ny) \exp\left[mc_{k_I} t + im \left(x - c_{k_R} t \right) \right] \qquad (3.4.9)$$

In complex polar coordinates this is equivalent to

$$\psi' = \sum_{k=1}^{3} \left| \hat{\psi}_k \right| \cos(ny) \, e^{mc_{k_I} t} \, e^{i(q_k - mc_{k_R} t)} \, e^{imx} \qquad (3.4.10)$$

in which $\left| \hat{\psi}_k \right| = (\hat{\psi}_{k_R}^2 + i\hat{\psi}_{k_I}^2)^{1/2}$ represents the modulus of the complex vector $\hat{\psi}_{k_R} + i\hat{\psi}_{k_I}$ and $q = \arctan(\hat{\psi}_{k_I} / \hat{\psi}_{k_R})$ is the vector angle from the positive real axis. Combining the modulus and amplification factor into one term $\hat{\psi}_k^* = \left| \hat{\psi}_k \right| \exp(mc_{k_I} t)$ and defining $q_k^* = q_k - mc_{k_R} t$ allows (3.4.10) to be rewritten as a single wave solution of the type

$$\psi' = \hat{\psi}_A \cos(ny) e^{i\psi_p} e^{imx} \tag{3.4.11}$$

where the amplitude $\hat{\psi}_A$ is

$$\hat{\psi}_A = \left[\left(\sum_{k=1}^{3} \hat{\psi}_k^* e^{iq_k^*} \right)_R^2 + \left(\sum_{k=1}^{3} \hat{\psi}_k^* e^{iq_k^*} \right)_I^2 \right]^{1/2}$$

$$= \left[\left(\sum_{k=1}^{3} \hat{\psi}_k^* \cos q_k^* \right)^2 + \left(\sum_{k=1}^{3} \hat{\psi}_k^* \sin q_k^* \right)^2 \right]^{1/2} \tag{3.4.12}$$

and the phase angle ψ_p is determined from

$$\psi_p = \arctan \frac{\left(\sum_{k=1}^{3} \hat{\psi}_k^* e^{iq_k^*} \right)_I}{\left(\sum_{k=1}^{3} \hat{\psi}_k^* e^{iq_k^*} \right)_R}$$

$$= \arctan \frac{\sum_{k=1}^{3} \hat{\psi}_k^* \sin q_k^*}{\sum_{k=1}^{3} \hat{\psi}_k^* \cos q_k^*} \tag{3.4.13}$$

In the same manner the remaining perturbation quantities θ', σ', ω', h' and η' may be described in a form similar to that of (3.4.12) with their respective amplitudes $\hat{\theta}_A$, $\hat{\sigma}_A$, $\hat{\omega}_A$, $\hat{h}_A$, $\hat{\eta}_A$ and phase angles θ_p, σ_p, ω_p, h_p, η_p. Calculations were carried out to determine these values as functions of time and for varying initial conditions as well as for different basic flow properties.

CHAPTER 4

NUMERICAL RESULTS AND DISCUSSION

4.1 Preliminary Comments

The present model, like that of Haltiner (1967)
incorporates a surface sensible heat flux but, unlike the
latter, it also allows for the inclusion of surface friction
effects, heat and momentum diffusion terms and a simple
meridional variation in the perturbation field. The
numerical investigations of the dynamic response
characteristics of the model for different states of current
flow are discussed first. These flow regimes are
indentified in the following manner:

 (i) Model 1. Adiabatic flow with no frictional
 vorticity terms included.

 (ii) Model 2. Sensible heating (including the
 redistribution of heat by thermal diffusivity)
 with no frictional vorticity terms.

 (iii) Model 3. Adiabatic flow with frictional
 vorticity terms included.

 (iv) Model 4. Sensible heating with frictional
 vorticity terms included.

As an initial simplification it is assumed in each of
the four 'models' that the perturbation field is not a
function of latitude. Later, a latitudinal dependence is
incorporated in conjunction with model 4 and the

calculations are redone. This particular version of the modelling is simply referred to as the 'full model'.

The latter part of this chapter focusses on the behavior of the longest waves. Of specific interest are those features of long waves which can be applied to blocking ridge development in the North Pacific.

4.2 Influence of Sensible Heating and Friction on Dynamic Stability Response

In order to compare the various model runs the steady-state atmospheric quantities were held constant unless otherwise noted with $U_r = 10$ m/s, $f(45N) = 1.0312 \times 10^{-4}$ s^{-1}, $\beta(45N) = 1.61 \times 10^{-11}$ m^{-1}s^{-1} and $\bar{\sigma} = 12^{\circ}$C. The phase velocity solutions of models 1 through 4 were then obtained from the corresponding cubic frequency equation. Since the frequency equation is solved in terms of $(c_k - U)$ it should be kept in mind that the real portion of any solution represents the phase velocity of the perturbation wave relative to the speed of the mean westerly wind.

Figures 4.1a and 4.1b show both the imaginary and real portions of the solutions $(c_k - U)$ as a function of wavelength L_x for models 1 and 2, respectively. Each case exhibits a neutral or near-neutral solution $(c_I \simeq 0)$ arbitrarily denoted I1, a damped solution $(c_I < 0)$ designated curve I2 and an unstable solution I3 $(c_I > 0)$. The corresponding real parts to these curves are shown as R1, R2 and R3.

Features apparent in the adiabatic-frictionless

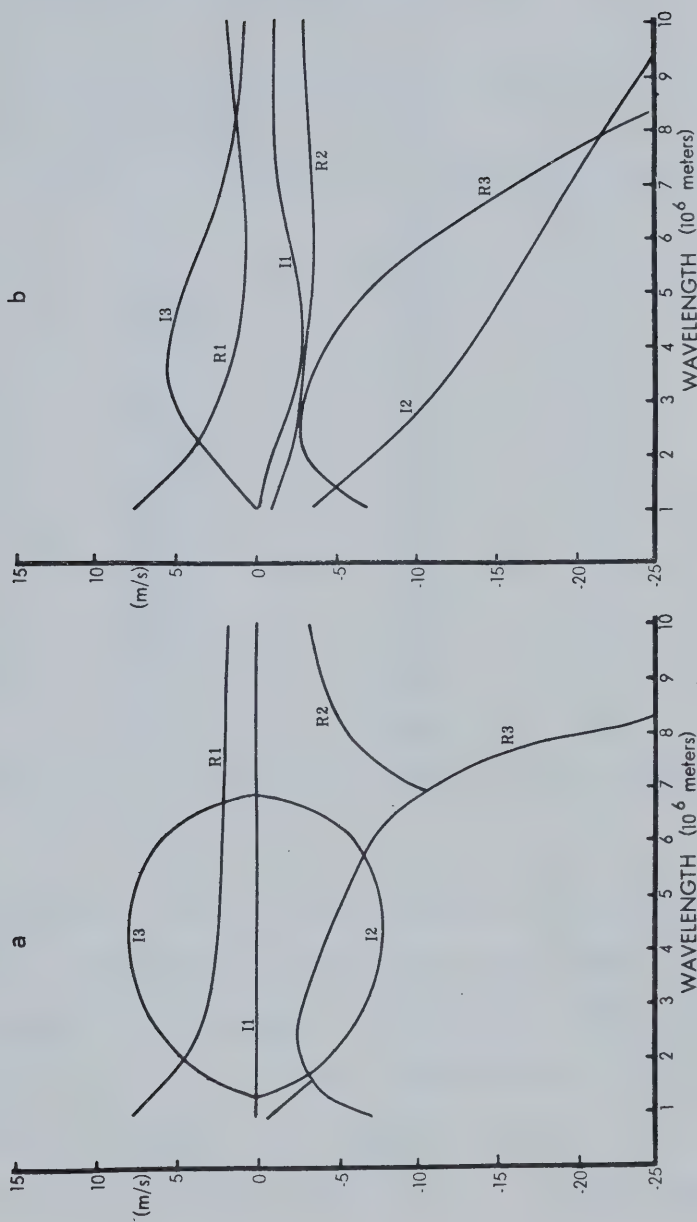Fig. 4.1. Response curves for (a) adiabatic-frictionless flow (model 1), and (b) diabatic-frictionless flow (model 2). Phase velocities (ordinate) are in meters per second with curves R_1, R_2 and R_3 the real parts and I_1, I_2 and I_3 the imaginary parts of the frequency equation solutions $(c_k - U)$, $k = 1, 2, 3$. Wavelengths (abscissa) are in units of 1000 km in the east-west direction.

Table 2.   Real (R3) and imaginary (I3) portions of the phase
velocities over the unstable waveband of Fig. 4.1a and the
corresponding e-folding times (t_e).

Wavelength (km)	R3 (m/s)	I3 (m/s)	t_e (days)
1000	-7.20	0.00	
1500	-3.29	2.05	1.35
2000	-2.80	4.50	0.82
2500	-2.73	5.99	0.77
3000	-3.00	6.95	0.80
3500	-3.49	7.53	0.86
4000	-4.14	7.82	0.94
4500	-4.93	7.86	1.06
5000	-5.83	7.66	1.20
5500	-6.86	7.16	1.42
6000	-7.99	6.27	1.76
6500	-9.23	4.74	2.52
7000	-11.01	0.00	

solutions of Fig. 4.1a are that the unstable and damped
waves propagated at the same speeds over the entire range of
unstable wavelengths. Furthermore, these speeds were always
slower than that of the mean westerly wind speed. The
neutral wave in turn always travelled faster than the zonal
wind speed as indicated by the R1 curve being positive at
all wavelengths.

Introduction of sensible heating to the model as shown
in Fig. 4.1b has diminished the amplitude of the I3 curve at

Table 3. Real (R3) and imaginary (I3) portions of the phase
velocities over the unstable waveband of Fig. 4.1b and the
corresponding e-folding times (t_e)

Wavelength (km)	R3 (m/s)	I3 (m/s)	t_e (days)
1000	-7.27	0.06	30.70
1500	-4.59	1.13	2.45
2000	-3.07	2.81	1.31
2500	-2.55	4.20	1.10
3000	-2.72	5.07	1.09
3500	-3.27	5.47	1.18
4000	-4.09	5.50	1.34
4500	-5.18	5.22	1.59
5000	-6.61	4.67	1.97
5500	-8.47	3.93	2.58
6000	-10.82	3.17	3.49
6500	-13.57	2.54	4.71
7000	-16.60	2.06	6.26
7500	-19.85	1.70	8.13
8000	-23.28	1.42	10.38
8500	-26.90	1.21	12.94
9000	-30.69	1.05	15.79
9500	-34.66	0.91	19.23
10000	-38.82	0.81	22.74
10500	-43.15	0.72	26.86
11000	-47.68	0.64	31.66
11500	-52.39	0.58	36.52
12000	-57.30	0.53	41.71

lower and intermediate wavelengths, but at the same time has extended the band of unstable wavelengths to beyond 10,000 km. Other changes from the values cf model 1 are that the I2 curve now shows much stronger damping at longer wavelengths and the R2 and R3 curves no longer coincide over any interval. The coefficient for surface heating in this case was chosen as $k_\ell = 10^{-2}$ J/(kg s °C) and, unless otherwise noted, this value was used in all calculations where heating was incorporated.

Haltiner's (1967) findings using the same value of surface heating and a vertical wind shear of 10 m/s over a 25 kPa layer show qualitatively the same shape as the curves of Fig. 4.1b. Tables 2 and 3 give the values for the unstable waveband at every 500 km for models 1 and 2 from the present study, while Haltiner's results are found in Table 4. The latter two tables are quite comparable over wavelengths from 3500 to 8000 km. Outside of this range the present model gave a slightly more unstable wave as indicated by the c_I values and the computed e-folding times.

The results of incorporating friction are presented in Fig. 4.2a. It is apparent that there are two regions at the extremes of the unstable waveband where increased instability occurred when compared with that of the adiabatic-frictionless case. The amount of broadening of the waveband at longer wavelengths was very small, however, when compared with Fig. 4.1b. It is also evident by comparison of Tables 2 and 5 that, except within these two

Table 4.   Real (R3) and imaginary (I3) portions of the phase
velocities over the unstable waveband of Haltiner (1967) for
sensible heating with no friction. (k_h = 10^{-2} J/(kg s $^{\circ}$C),
r = 2, U_T = 10 m/s and $\bar{\sigma}$ = 15°C over a 25 kPa layer)

Wavelength (km)	R3 (m/s)	I3 (m/s)	t_e (days)
1000	-8.39	0.00	
1500	-6.31	0.24	11.51
2000	-4.45	2.06	1.79
2500	-4.03	3.49	1.32
3000	-4.06	4.44	1.24
3500	-4.44	5.03	1.28
4000	-5.12	5.30	1.39
4500	-6.07	5.30	1.56
5000	-7.30	5.04	1.83
5500	-8.85	4.55	2.28
6000	-10.80	3.88	2.85
6500	-13.19	3.10	3.86
7000	-16.04	2.37	5.44
7500	-19.27	1.78	7.76
8000	-22.76	1.36	10.84
8500	-26.45	1.06	14.77
9000	-30.31	0.85	19.50
9500	-34.34	0.69	25.36
10000	-38.54	0.58	31.76
10500	-42.92	0.49	39.47
11000	-47.47	0.42	48.24
11500	-52.21	0.36	58.84
12000	-57.14	0.31	71.31
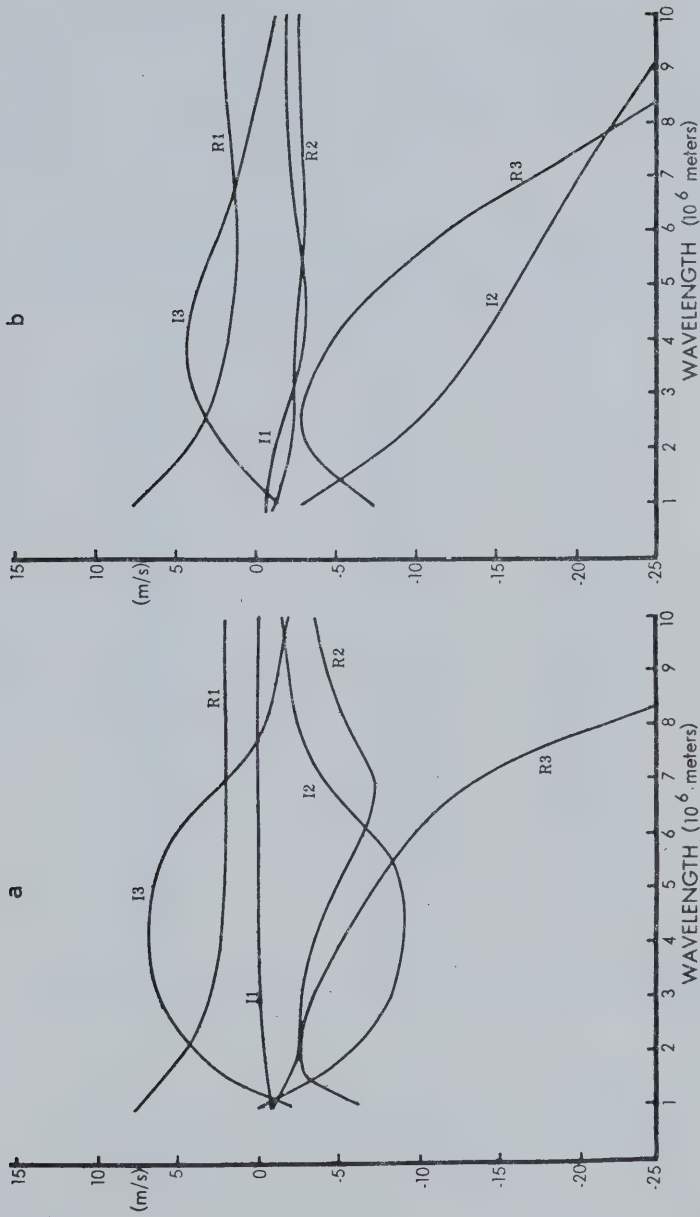
Fig. 4.2. Response curves for (a) adiabatic flow with friction included (model 3), and (b) conditions of diabatic heating with friction included (model 4). Phase velocities (ordinate) are in meters per second with curves R_1, R_2 and R_3 the real parts and I_1, I_2 and I_3 the imaginary parts of the frequency equation solutions $(c_k - U)$, $k = 1,2,3$. Wavelengths (abscissa) are in units of 1000 km in the east-west direction.

narrow regions, the amplitude of the I3 curve has everywhere been reduced.

Table 5.   Real (R3) and imaginary (I3) portions of the phase velocities over the unstable waveband of Fig. 4.2a and the corresponding e-folding times (t_e).

Wavelength (km)	R3 (m/s)	I3 (m/s)	t_e (days)
1000	-1.60	-8.23	
1500	-2.66	1.45	1.91
2000	-2.82	3.68	1.00
2500	-3.03	5.11	0.90
3000	-3.50	6.04	0.92
3500	-4.17	6.59	0.98
4000	-4.98	6.86	1.07
4500	-5.92	6.88	1.21
5000	-6.98	6.65	1.39
5500	-8.18	6.15	1.65
6000	-9.54	5.29	2.09
6500	-11.19	3.93	3.05
7000	-13.66	1.91	6.75
7500	-17.55	0.28	49.34
8000	-21.63	<0	

The response curves of model 4 containing both sensible heating and friction are given in Fig. 4.2b. A longwave cutoff is now found near 8500 km, roughly 1500 km longer than the cutoff shown for adiabatic-frictionless conditions. It is also significant that over the unstable waveband the

R3 values of Fig. 4.2b imply much lower propagation rates
than found initially in Fig. 4.1a. For instance, a mean
wind of U=15 m/s would mean that every unstable wave in
model 1 would propagate eastward as it amplified. With the
inclusion of both sensible heating and friction this value

Table 6.   Real (R3) and imaginary (I3) portions of the phase
velocities over the unstable wave band of Fig. 4.2b and the
corresponding e-folding times (t_e).

Wavelength (km)	R3 (m/s)	I3 (m/s)	t_e (days)
1500	-3.11	<0	
2000	-2.81	1.70	2.17
2500	-3.17	3.08	1.50
3000	-3.89	3.94	1.40
3500	-4.89	4.31	1.50
4000	-6.14	4.33	1.70
4500	-7.71	4.06	2.04
5000	-9.63	3.56	2.59
5500	-11.92	2.93	3.46
6000	-14.53	2.25	4.91
6500	-17.43	1.61	7.44
7000	-20.56	1.04	12.40
7500	-23.91	0.54	25.59
8000	-27.45	0.10	147.37
8500	-31.19	<0	

for the mean wind would result in a stationary unstable wave
of about 6000 km (Table 6) while at longer wavelengths

unstable wave growth could occur as the wave retrogressed westwards. The implications of this will be investigated further in the discussion on blocking ridge development.

The rate of surface sensible heat exchange and the degree of surface friction have as yet been held constant. Figure 4.3 illustrates the change in the unstable curve for model 2 under various rates of surface heating. The basic flow parameters were unchanged from the values used earlier. It is seen that increasing the surface heat input resulted in a further reduction of the curve amplitude at lower and intermediate wavelengths. Conversely the region at longer wavelengths exhibited increased instability. It is also noticeable that the region of enhanced instability between successive increments in the value of k_t was gradually shifted to longer wavelengths, indicating that further increases in the heating rate would result in greater instability at extremely long waves only.

Increasing the degree of surface friction through the coefficient k_s in model 3 resulted in only marginal increases in the amount of instability at the edges of the unstable waveband. However, in changing k_s from 4×10^{-6} to 10^{-5} s^{-1} a fairly significant reduction in the amplitude of the I3 curve did occur at intermediate values of the wavelength range.

4.3 Variation of the Steady-state Flow Parameters

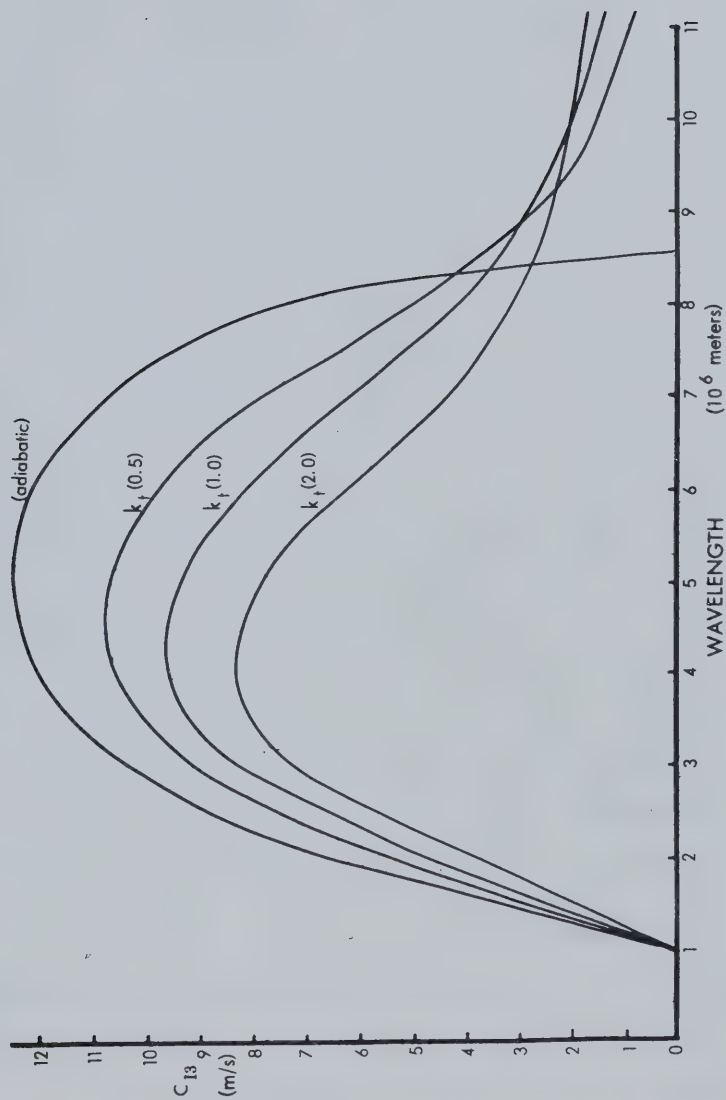The response values of the perturbation field are

Fig. 4.3. Response of the stability curve c_{I3} to different surface sensible heating rates. The diabatic curves, taken from model 2, are labelled with the value of the surface sensible heating coefficient k_t (10^{-2} J/(kg s °C)) used in the calculations. The adiabatic curve is from model 1.

affected if certain properties of the steady-state flow change. This is easily seen in the case of a change in the zonal wind U. Since U appears as part of the real portion of the frequency equation solution it does not influence the stability of the waves. Its main influence is to define the 'absolute' speed of the waves on the x-axis and a change in U results in a corresponding shift of these values. This is important because the value assigned to U will play a major role in determining whether it is possible to have a stationary wave within the unstable band of wavelengths.

The mean vertical wind shear U_T is a measure of the baroclinicity of the basic state and the numerical results indicated that the greater the shear the greater the possible instablity of the perturbations in the flow. The solid curves of Fig. 4.4 represent the change in stability experienced in model 4 under the same conditions as employed earlier except that U_T was varied. With greater wind shear the instability of the I3 curve was increased at all wavelengths. The effect on the real portion of the unstable solution was to decrease the speed of the waves by a few meters per second. In general very little instability was observed in any of the model types at wavelengths greater than 6000 km until the wind shear had exceeded 5-6 m/s. Thus, at low mid-tropospheric wind shear values the possibility of longwave instability is small.

Figure 4.4 also shows the effect on the I3 curve of changing the mean static stability. As the mean stability
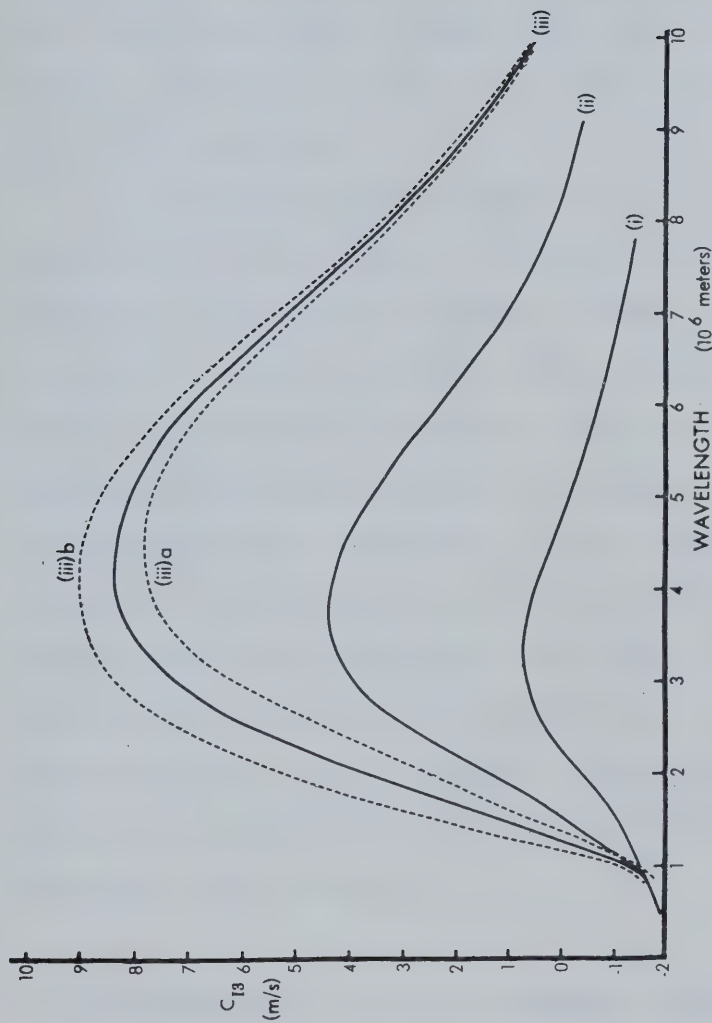
Fig. 4.4. Response of the stability curve c_{I3} to changes in the mean wind shear and mean static stability. The solid curves are for a constant static stability of $\bar{\sigma} = 12^{\circ}C$ with vertical wind shear values of (i) 5 m/s, (ii) 10 m/s and (iii) 15 m/s. The dashed curves have a constant vertical shear of $U_T = 15$ m/s for mean static stabilities of (iii)a $15^{\circ}C$ and (iii)b $9^{\circ}C$. All calculations were taken from model 4 with all other quantities kept constant.

of the atmosphere was increased the instability of the
perturbation field was reduced. This reduction is much more
significant at the lower end of the wavelength range and
became marginal at larger L_x values. The relative
propagation rate of shorter waves was also found to decrease
as $\bar{\sigma}$ was increased, but once again this effect diminished at
longer wavelengths to the point where the wave speeds were
virtually unchanged.

Although the perturbations have been assumed to be
latitudinally independent, variations in latitude may still
influence the numerical results through the Coriolis
parameter and its meridional derivative β. Therefore, the
values of these two quantities were varied so as to
represent different latitudinal x-axes. At lower latitudes,
as suggested by a comparison of the unstable curves in
Fig. 4.5, the perturbation field was found to be
considerably more stable and the range of unstable
wavelengths was reduced significantly. In addition,
Fig. 4.5 shows that as latitude decreased the perturbation
waves had a greater rate of retrogression with respect to
the mean zonal current.

4.4 Perturbation Field as a Function of Latitude

At this time the previous assumption that the
perturbation field is independent of latitude is relaxed and
the simple cosine variation of (3.3.2) is employed. Unlike
wavelengths on the x-axis which have been expressed in
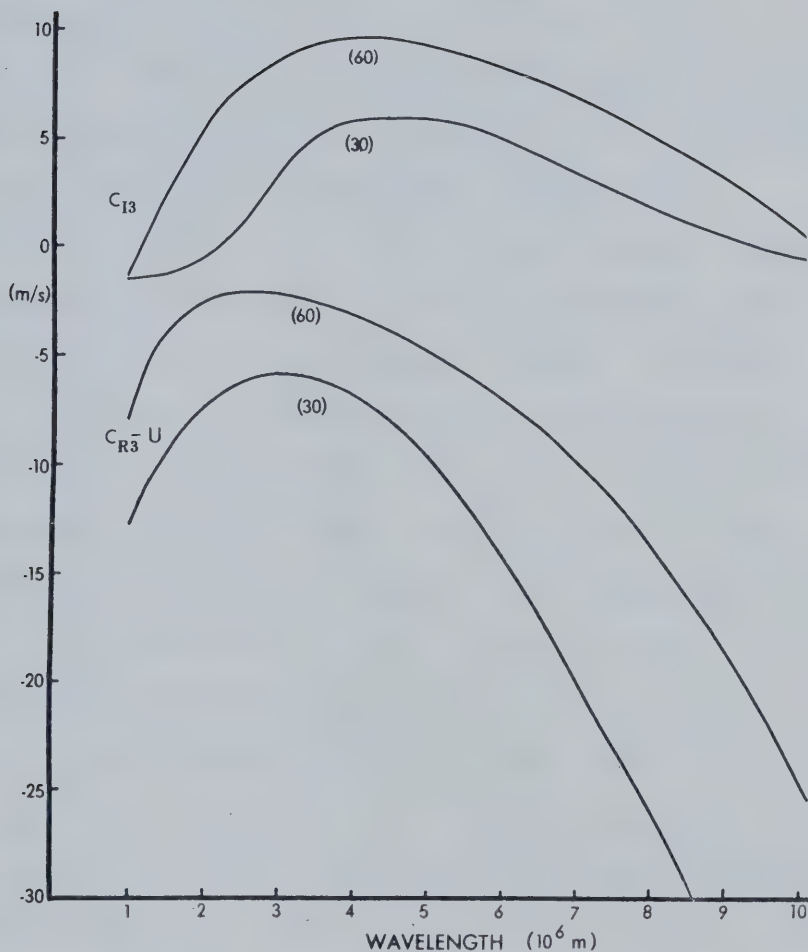
Fig. 4.5. Effect of latitude variations on the stability and propagation rates of unstable waves. The stability curves c_{I3} and relative wavespeed curves c_{R3} - U were computed using model 4 with U_T = 15 m/s. Latitude is distinguished by the bracketed values assigned to each curve. In the calculations f(60N) = 1.263 x 10^{-4} s^{-1}, β(60N) = 1.14 x 10^{-11} m^{-1} s^{-1}, f(30N) = 7.292 x 10^{-5} s^{-1} and β(30N) = 1.98 x 10^{-11} m^{-1} s^{-1}.

distances of meters or kilometers a meridional wavelength will be given in terms of degrees of latitude. In all cases the origin in the north-south direction will be taken as 45N. The interpretation of $L_y=120°$ is that of a perturbation travelling in an east-west direction having its maximum absolute amplitude at y(45N)=0 and an amplitude which approaches zero at latitudes 75N and 15N.

The computations were redone using the same numerical values as utilized earlier for the steady-state quantities. The full model was run for varying values of $n=2\pi/L_y$. Figure 4.6 shows the phase-velocity response curves (c_k-U) at latitude 45N when $L_y=90°$. The general shapes of the curves were similar to those shown in Figures 4.1 and 4.2. A comparison of values in Tables 6 and 7 indicates that unstable long waves have greater rates of growth and travel at slower propagation rates after the 90° latitudinal dependence has been introduced into the modelling.

Figure 4.7 illustrates the resulting unstable solution for a range of L_y values between 60° and ∞ ($L_y=\infty$ implies no latitude dependence). The changes that occurred in the c_{r3} values in response to varying values of L_y were similar and, therefore, not all of these curves are shown. In going from $L_y=\infty$ to $L_y=60°$ the amplitude of the c_{r3} curve showed a marginal decrease in amplitude up to a wavelength of $L_x=5000$ km. At wavelengths $L_x>5000$ km instability increased and, as a result, the unstable waveband was extended to include longer waves. The relative travelling speeds of the
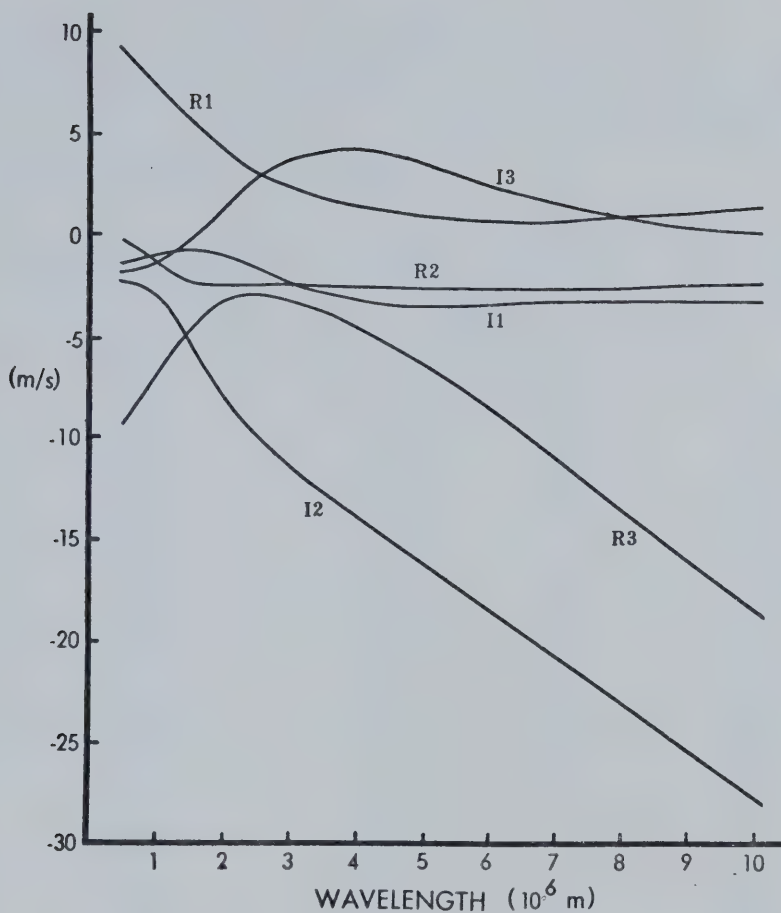
Fig. 4.6. Phase velocity response for the full model incorporating a 90° latitudinal dependence ($L_y = 90^{\circ}$). Curves R_1, R_2 and R_3 are the real parts and I_1, I_2 and I_3 the corresponding imaginary parts to the frequency equation solutions ($c_k - U$), $k = 1, 2, 3$.

Table 7.   Real (R3) and imaginary (I3) portions of the phase
velocities over the unstable waveband of Fig. 4.6 and the
corresponding e-folding times (t_e).

Wavelength (km)	R3 (m/s)	I3 (m/s)	t_e (days)
1500	-4.34	<0	
2000	-3.18	1.54	2.39
2500	-2.80	2.84	1.62
3000	-3.03	3.68	1.50
3500	-3.58	4.10	1.57
4000	-4.31	4.20	1.75
4500	-5.17	4.08	2.03
5000	-6.14	3.81	2.42
5500	-7.22	3.43	2.95
6000	-8.39	2.99	3.70
6500	-9.64	2.54	4.71
7000	-10.94	2.11	6.11
7500	-12.25	1.70	8.13
8000	-13.55	1.33	11.08
8500	-14.82	1.00	15.66
9000	-16.05	0.69	24.03
10000	-17.24	0.41	44.93
10500	-18.37	0.15	128.94
11000	-19.44	<0	
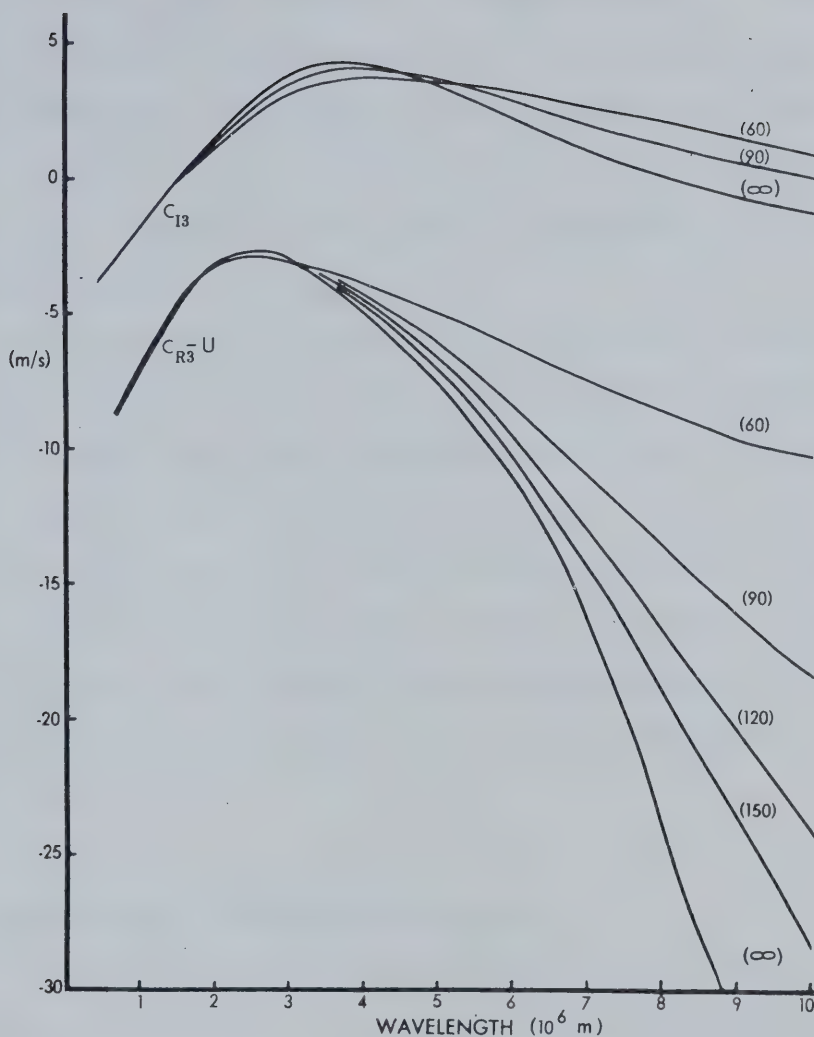
Fig. 4.7. Effect of variations in the meridional wavelength L_y on the stability and propagation of unstable waves. Numerical results for the stability curves c_{I3} were computed using the full model and $L_y = 60°$, $90°$ and ∞ as indicated by the bracketed values assigned to each curve. For the relative wavespeed curves the scope of L_y values was expanded to include $L_y = 120°$ and $150°$. The curves for $L_y = \infty$ are interpreted as having no latitudinal dependence and are, therefore, analogous to curves of model 4.

unstable waves were affected in a similar manner. Up to values of L_x =4000 km the propagation rates of the waves were almost unchanged. At values greater than 4000 km reductions in the magnitude of L_y resulted in the waves experiencing propagation rates which more closely approached the speed of the steady-state current.

If y is taken to be non-zero in the model then the absolute amplitude of the perturbation field is reduced. This in itself has little bearing on the dynamic stability of the flow if the ratio y/L_y is less than 1/4 (i.e. if $y/L_y \simeq$ 1/4 then $\tan(ny) \to \infty$ in the coefficient b^{15}). A value of y≠0, however, implies higher or lower latitudes and the main changes in the relative phase velocity curves occur because of changes in f and β as was seen previously in Fig. 4.5.

4.5 Amplitude and Phase Relationships

Phase velocity solutions to the frequency equation determine the stability features of the perturbation field. However, stability curves do not show directly the interactions of the three wave solutions or the relationships between the various perturbation quantities. The initial-value technique outlined in Chapter 3 will now be used to extend the analysis to include such interactions and interelationships. The following parameters were held constant: U=20 m/s, U_T =10 m/s, L_y =90°, k_t =10⁻² J/(kg s °C), $\bar{\sigma}$=12°C, k_s =4X10⁻⁶ s⁻¹, K_M =K_H =10⁵ m²/s and k_i =k_h =10⁻⁶ s⁻¹

with f and β evaluated at a latitude of 45N. In addition, the initial amplitudes assigned to the stream function, potential temperature and static stability perturbation waves were held constant at $\hat{\psi}_o$ =9.806X10⁶ m²/s, $\hat{\theta}_o$ =10°C and $\hat{\sigma}_o$ =2°C. In order to obtain estimates of the magnitude of the stream function it is useful to assume from the linear balance equation that $\hat{\phi}_o = \hat{\psi}_o \bar{f}/g$ where the mean Coriolis parameter can be taken as being approximately 10⁻⁴ s⁻¹. Therefore, the averaged value of the stream function can be though of in terms of a geopotential height with an initial amplitude of 100 m. In the future $\hat{\psi}_A$ will be expressed in its geopotential 'equivalent' in units of meters.

Figures 4.8 and 4.9 show the characteristic curves for a wavelength of 4000 km taken from model 4. The initial phase angles ε_θ and ε_σ in Fig. 4.8 were both taken to be 90° meaning that the potential temperature and stability waves lagged behind the stream function. These angles were changed to -90° in Fig. 4.9. The 4000 km wavelength is indicative of the middle range of the instability waveband where growth rates are quite large.

The rate of amplification for the different perturbation quantities as displayed in Fig. 4.8a was quite rapid during a 72-hour period. It is also apparent that, except for a time during the first 12 hours when the amplitude of the static stability briefly decreased, the amplification rate of each perturbation increased in time.

Figure 4.8b displays all phase angles in degrees. If a

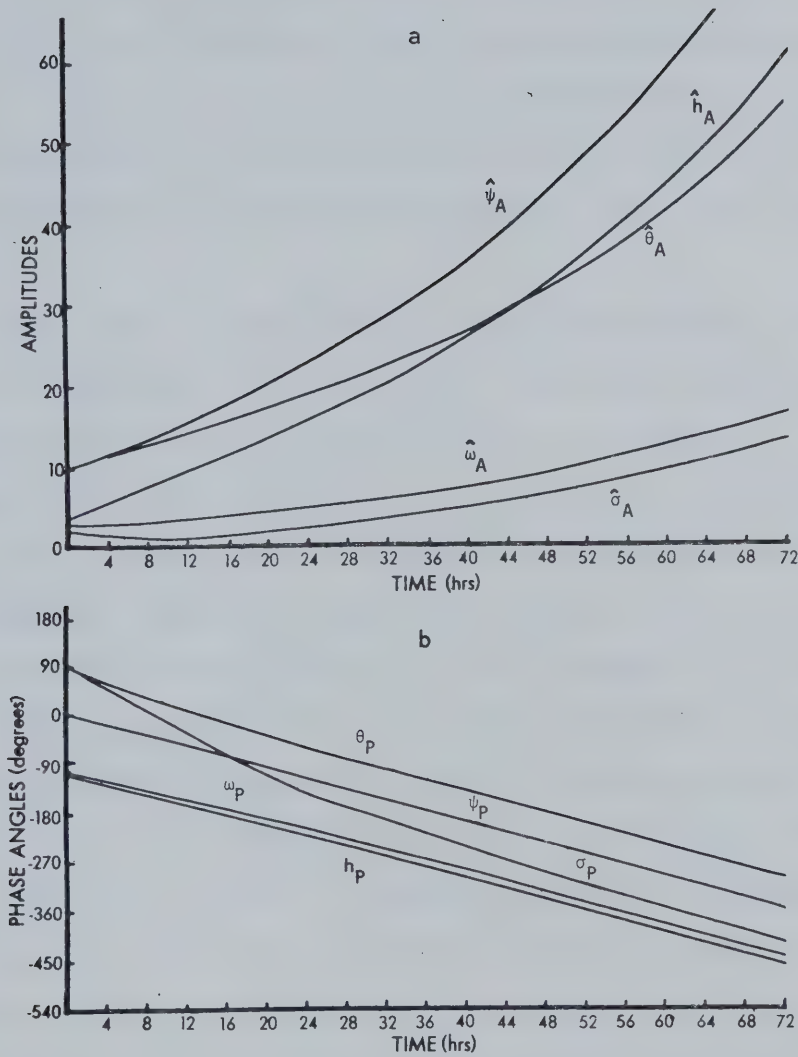Fig. 4.8. Perturbation amplitudes and phase angles as functions of time for model 4 with $L_x = 4000$ km, $U = 20$ m/s, $U_T = 10$ m/s, $\varepsilon_\theta = 90°$ and $\varepsilon_\sigma = 90°$. Amplitudes in (a) are $\hat{\psi}_A (10^1 m)$, $\hat{\theta}_A (°C)$, $\hat{\sigma}_A (°C)$, $\hat{\omega}_A (10^{-4} \text{ kPa/s})$ and $\hat{h}_A (10^{-2} \text{ J/(kg s)})$. Phase angles in (b) are in degrees.

curve slopes towards lower (negative) phase angle values the
wave in question is progressing in an easterly direction. A
slope to higher (positive) phase angles thus represents
retrogression westwards. All of the perturbation waves
depicted in this figure travelled eastwards and the short
interval when $\hat{\sigma}_A$ is damped is seen to correspond to a time
when the static stability wave advanced toward the stream
function.

The growth curves for Fig. 4.9a are slightly changed
from those of the previous case. The stream function was
damped initially for 24 hours while the potential
temperature wave advanced to within a lag of approximately
130° (Fig. 4.9b), after which the stream fuction began to
amplify. In addition, the former wave's eastward motion was
reduced substantially between 12 and 24 hours until the
potential temperature wave had moved into this appropriate
lag position. The potential temperature wave can be
interpreted as a 'thermal' wave since it uniquely determines
the value of η' which is representative of a geopotential
thickness in the same manner that ψ' is representative of
height. Thus, the thermal wave necessarily lags the
geopotental height wave in order for amplification of the
height field to occur. Static stability increased during
this initial time period and then subsequently showed a
short period of damping. A large drop in the surface
heating amplitude was noticed during the first few hours as
this wave moved rapidly from a trailing position behind the

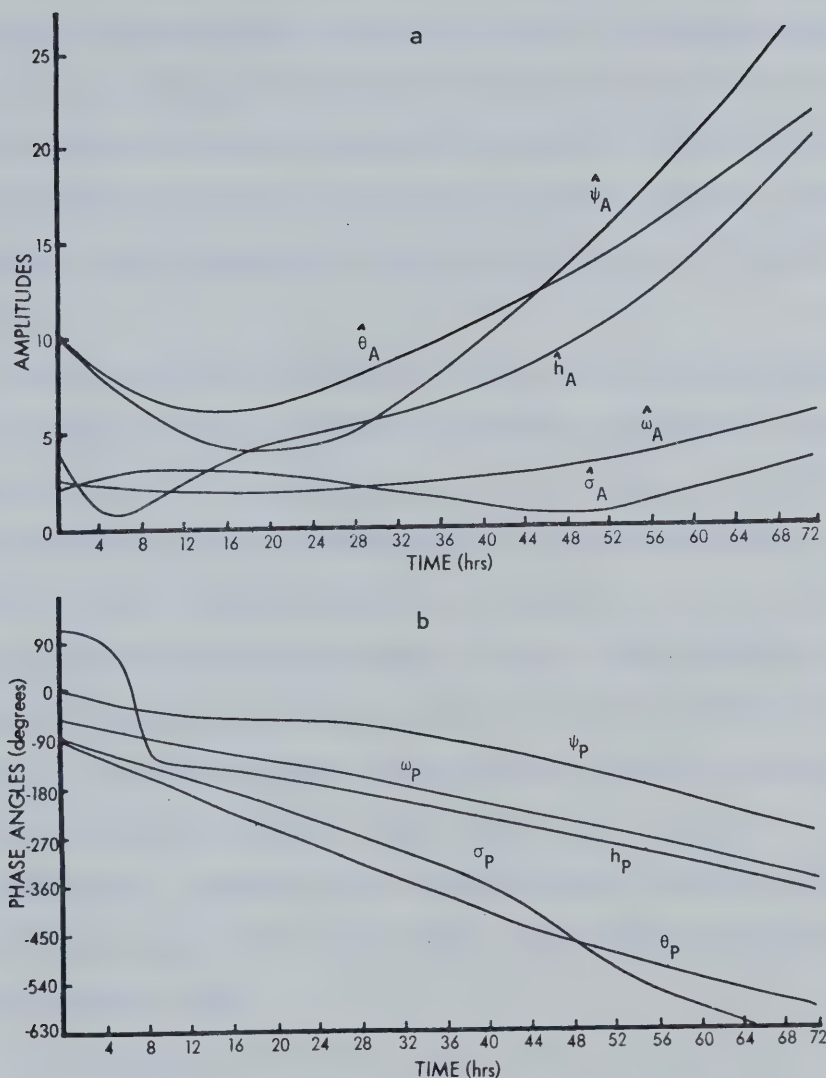Fig. 4.9. Perturbation amplitudes and phase angles as functions of time for model 4 with L_x = 4000 km, U = 20 m/s, U_T = 10 m/s, $\varepsilon_\theta = 90^\circ$ and $\varepsilon_\sigma = -90^\circ$. Amplitudes in (a) are $\hat{\psi}_A (10^1 m)$, $\hat{\theta}_A (^\circ C)$, $\hat{\sigma}_A (^\circ C)$, $\hat{\omega}_A (10^{-4}$ kPa/s) and $\hat{h}_A (10^{-2}$ J/(kg s)). Phase angles in (b) are in degrees.

stream fuction wave into a phase lead.

Many runs were made with L_x=4000 km for different
values of $\mathcal{E}_\theta$, $\mathcal{E}_\sigma$ and with various model types. The
adiabatic-frictionless results of model 1 corresponding to
the two cases already discussed have qualitatively the same
growth and phase relations as when friction and sensible
heating are included. In general, however, model 1 gave the
greatest amplification of the waves during the 72-hour
period.

Certain phase difference values showed characteristic
changes depending on whether heating or frictional effects
were included in the modelling. As an example, in Fig. 4.8b
the difference $\theta_p - \psi_p$ at the end of 72 hours was 56°. In
model 2, using the same initial conditions, this phase
difference was 63° while model 1 gave a final value of 73°.
Thus, friction and sensible heating had the effect of
allowing the thermal wave to approach a position somewhat
closer behind the geopotential height wave during
amplification. Other runs using different initial phase
conditions values also supported these trends between the
various model types.

More pronounced changes were seen in the values of
$\sigma_p - \psi_p$. In Fig. 4.8b the static stability overtook the
stream function in 12 hours after which it slowly moved to a
56° lead by t=72 hr. Adding a 90° latitudinal dependence in
the full model did not alter this value and dropping
friction from the modelling resulted in only a 5° decrease

in the phase difference. Model 1, however, had a final
phase lead value of 114°, a rather significant change which
can be attributed to the lack of sensible heating. Once
more this trend was supported in other runs with various
initial conditions.

The surface heating and vertical velocity perturbation
fields showed evidence of having consistent phase relations
with the stream function. Surface sensible heating was
found to lead the stream function during maximum growth of
the waves by a phase angle of 108-114°. This would put the
maximum heat input from the earth's surface to the
atmosphere in a position upstream of the trough position and
the zone of maximum cooling upstream of the ridge during
amplification.

In those instances when friction was not included in
the modelling the vertical velocity wave led the stream
function by approximately 102° indicating that maximum
downward velocities in the mid-troposphere occurred between
the ridge and the downstream trough position. When friction
was added this phase lead was reduced by 4 or 5 degrees.

Figures 4.10 and 4.11 show the curves for a wavelength
of L_x=7000 km. Such a wavelength is representative of long
waves where the degree of instability is decidedly less than
that of intermediate wavelengths near 4000 km. In both
cases shown the initial phase angles were 90°. Figure 4.10
illustrates model 4 while Fig. 4.11 pertains to the full
model.

Fig. 4.10. Perturbation amplitudes and phase angles as functions of time for model 4 with L_x = 7000 km, U = 20 m/s, U_T = 10 m/s, $\varepsilon_\theta = 90^\circ$ and $\varepsilon_\sigma = 90^\circ$. Amplitudes in (a) are $\hat{\psi}_A (10^1 m)$, $\hat{\theta}_A (^\circ C)$, $\hat{\sigma}_A (^\circ C)$, $\hat{\omega}_A (10^{-4}$ kPa/s) and $\hat{h}_A (10^{-2}$ J/kg s)). Phase angles in (b) are in degrees.

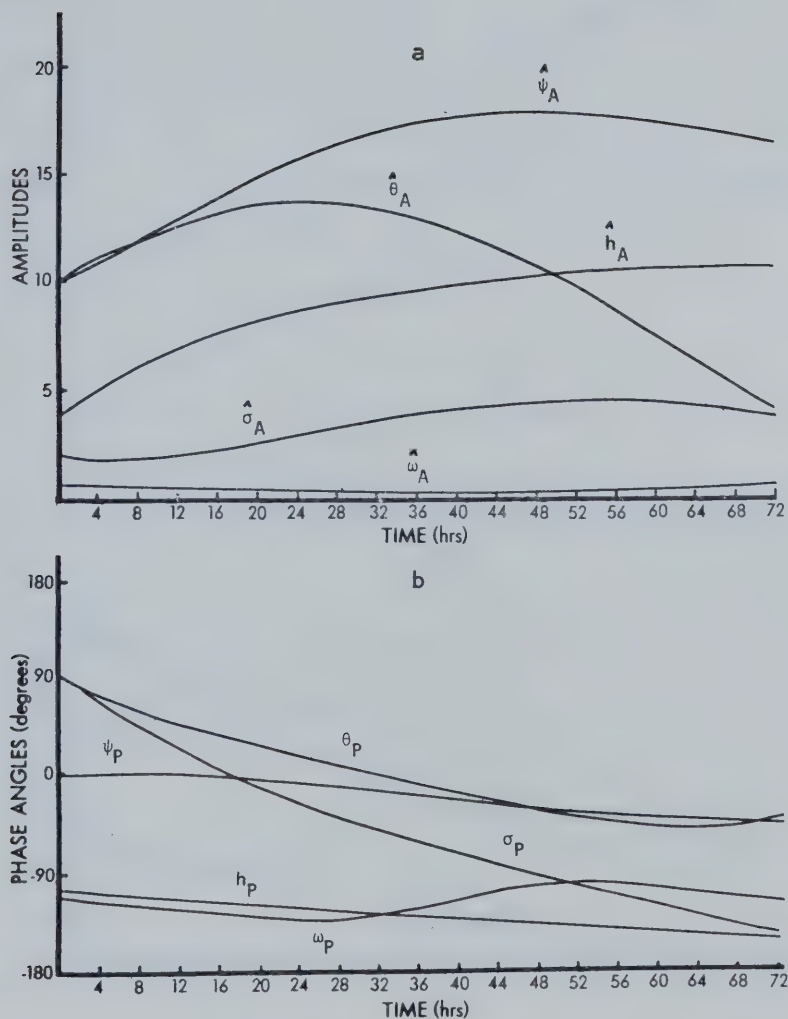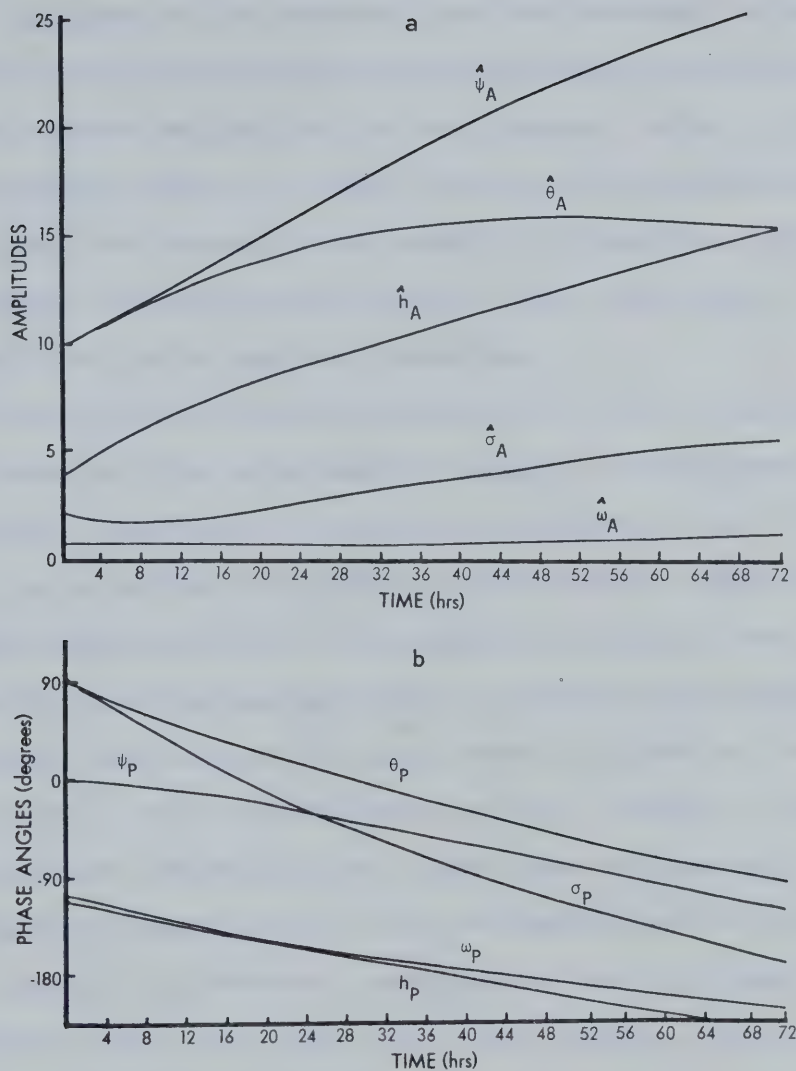Fig. 4.11. Perturbation amplitudes and phase angles as functions of time for the full model with $L_y = 90°$, $L_x = 7000$ km, $U = 20$ m/s, $U_T = 10$ m/s, $\varepsilon_\theta = 90°$ and $\varepsilon_\sigma = 90°$. Amplitudes in (a) are $\hat{\psi}_A(10^1 m)$, $\hat{\theta}_A(°C)$, $\hat{\sigma}_A(°C)$, $\hat{\omega}_A(10^{-4}$ kPa/s$)$ and $\hat{h}_A(10^{-2}$ J/(kg s)$)$. Phase angles in (b) are in degrees.

Several noteworthy differences are seen in these curves when they are compared with the previous results for $L_x = 4000$ km. As expected the perturbations now underwent a far lesser rate of growth than seen previously and they moved at slower speeds as depicted by the shallower slope to the phase angle curves. As well, the rate of amplification of the waves now generally decreased with time and, in some instances, as illustrated in Fig. 4.10b, the waves experienced retrogressive tendencies.

The first perturbation quantity to show a decrease in amplitude in Fig. 4.10a was the potential temperature. This occurred, according to the phase relations of Fig. 4.10b, when the potential temperature wave moved to within 20-25° of the stream function wave position. Then, as the potential temperature proceeded to overtake the stream function, the value of $\hat{\psi}_A$ also showed a reduction in amplitude. This is consistent with the concept of the thermal wave overtaking the height wave and thereby terminating amplification. In the latter part of the 72-hour period the potential temperature wave continued steadily moving away from the stream function which in turn began to retrogress slowly.

Previously the perturbation field with $L_x = 7000$ km was observed to have greater instability and faster propagation rates once a meridional variation was inserted into the modelling. These features are now reflected in Figs. 4.11a and 4.11b where by t=72 hours the perturbation quantities

had all undergone greater amplification and had progressed
further east than in the preceding case. The increased
amplification is the result of the fact that the potential
temperature never quite overtook the stream function wave
and maintained a minimum lag of 22°.

Changing the initial phase angles when $L_x = 7000$ km
invoked much the same behavior in the phase angle and
amplitude curves as was observed with the shorter wavelength
of 4000 km. Greater amplification was found to occur when
$\mathcal{E}_\theta$ was taken to be positive (lag) and $\mathcal{E}_\sigma$ negative (lead)
rather than reversing this arrangement. Of those numerical
computations performed where sensible heating was included,
the longer 7000 km waves showed the greatest amplification
rates when $\mathcal{E}_\theta$ was 180°. This arrangement implies that the
thermal wave is initially exactly out of phase with the
stream function wave and thus a warm trough and cold ridge
structure is present.

In most cases 72 hours was not enough time to establish
any definite phase relationship between the static stability
and stream function for the longer 7000 km wave. During
times of steady increases in $\hat{\psi}_A$ the vertical velocity wave
was found typically to precede the stream function wave by
125° to 155°. This lead was shortened to as little as 60°
when the stream function experienced weaker rates of growth
or underwent slight damping. It should also be noted that
the magnitude of the vertical velocity field was almost an
order of magnitude less than that found at the shorter

wavelength $L_x = 4000$ km. The surface heating wave tended to
remained downstream of the ridge position in the
calculations with a leading phase angle of 120° to 130° with
respect to the stream function wave.

At wavelengths longer than 7000 km the perturbation
field continued its trend to slower growth and greater
retrogressive motion. The 72-hour period of calculations
was insufficient to determine many consistent phase
relationships between the quantities although the behavior
of the waves is somewhat similar to the $L_x = 7000$ km results.

4.6 Blocking Ridge Development Over the North Pacific

Blocking ridge activity, as interpreted by Rex (1950a),
exhibits several distinguishing characteristics in its mid-
tropospheric flow. These characteristics were defined as:

> (i) a sharp transition from more or less zonal
> westerlies upstream to a meridional type of
> flow downstream must occur with a block;
>
> (ii) the basic westerly flow should have split
> into two branch streams with each branch
> transporting appreciable mass; and
>
> (iii) the two-jet pattern must exist with an
> extension of 45° of longitude or more
> downstream from the split and must persist for
> a minimal ten days.

As an example of such ridging occurrences a detailed case
study of an Atlantic block was presented in the Rex (1950a)
investigation. This particular ridging lasted for more than
20 days of which the first week could be described as being
the growth time required to develop a recognizable block

from a basic zonal flow.

In subsequent investigations Rex (1950b,1951) found that blocking showed a seasonal and spatial preference for its formation; preferring the winter months over that of the summer and an ocean environment over that of a continental location. He also determined that blocking normally persisted for 2 to 3 weeks after its formation with very little overall motion during its entire lifetime.

Whereas Rex employed daily synoptic charts in his studies, White and Clark (1975) used monthly mean data to investigate the occurrence of blocking activity over the North Pacific. This precluded the authors' ability to determine specific growth or duration times for blocking and it could only be established that the blocking had occurred long enough to have affected the mean monthly pressure pattern in the mid-troposphere. In defining what was considered as an oceanic block this study excluded all ridging waves which formed and were centered over the western part of North America as being a form of amplified mountain waves.

Some of White and Clark's results have been mentioned in Chapter 1. As shown in Fig. 4.12 the data revealed a preference for winter blocks which had a characteristic wavelength of 6000 to 7000 km centered over a longitudinal position of 160W to 170W. The blocking activity was also found rarely to exceed two months in length at any given period of the year and was apatially correlated with
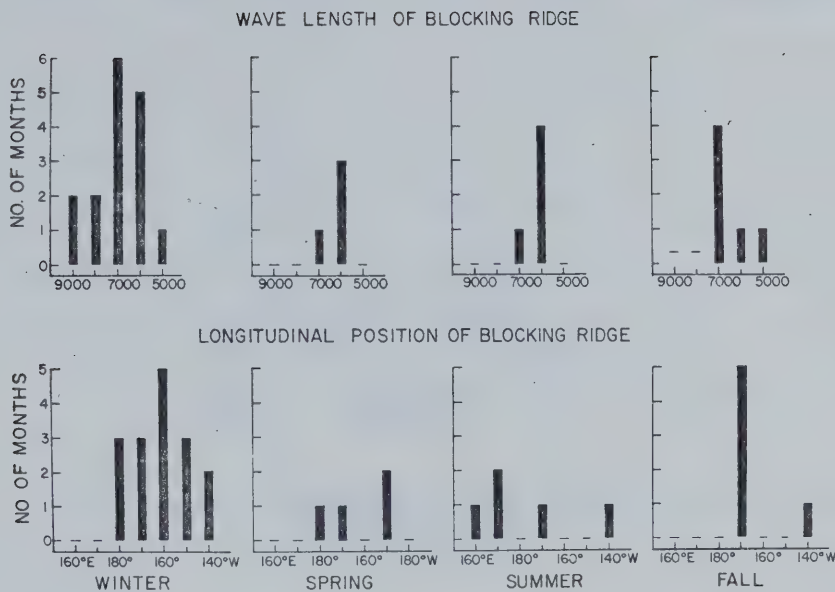
Fig. 4.12. Seasonal and spatial variability of North Pacific blocking ridges as given by White and Clark (1975). The histograms were based on monthly mean data over a period from 1950 to 1970. The seasons were defined as being; winter (January-March), spring (April-June), summer (July-September) and autumn (October-December).

patterns of anomalous surface sensible heat flux (cooling under the ridge position). It was the authors' conclusion that Haltiner's (1967) predictions of slow moving or stationary unstable longwave growth explained some of these observations and, therefore, supplied theoretical support for their findings. However, upon closer look at the argument presented there would seem to have been some misinterpretation of Haltiner's results on their part.

During their discussion White and Clark presented Fig

4.13 as Haltiner's unstable phase velocity solutions for
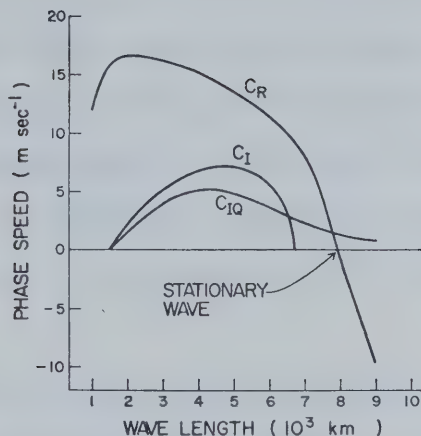
Fig. 4.13. The real (C_R) and complex (C_I) parts of the phase speed for baroclinic unstable waves as appeared in White and Clark (1975). The diabatic and adiabatic stability curves are denoted by C_{IQ} and C_I, respectively. Values are based on Haltiner's (1967) numerical results. The mean vertical wind shear and mean zonal wind were given as U_T = 10 m/s and U = 30 m/s in White and Clark's discussion; however, Haltiner's theory utilized a mean zonal wind of only 20 m/s in obtaining these curves.

U=30 m/s, U_T =10 m/s and conditions with sensible heat transfer and without. In reality these curves are obtained for a mean zonal wind of only 20 m/s. It is also left to interpretation in the White and Clark study that the real portion of the phase velocity (C_R) of Fig. 4.13 applies to both the adiabatic and diabatic cases. This is misleading

since the C_R curve shown is valid only for the adiabatic case. The diabatic version of this curve for U=20 m/s gives a stationary wave of approximately 7600 km which is some 300 to 400 km shorter than the 8000 km found for the adiabatic curve. If U is taken to be 30 m/s as is used throughout the White and Clark discussion, the diabatic model as indicated in Table 4 gives a stationary unstable wave of L_x=9000 km. This would then be well beyond the 8000 km value shown in Fig. 4.13.

The behavior of Haltiner's amplified waves has been likened to that of Rossby-type waves. The Rossby dispersion relation of;

$$L_s = 2\pi \left(\frac{U}{\beta}\right)^{1/2} \qquad (4.6.1)$$

might therefore be used to predict the wavelength, L_s, of a stationary Rossby-type wave. Applying (4.6.1) with U=30 m/s and β(45N)=1.61X10^{-11} m^{-1}s^{-1} gives a predicted L_s value of 8577 km. If U=20 m/s is substituted into the relation the stationary wavelength diminishes to 7003 km. Neither of these values agrees with a value of 7600 km claimed by White and Clark using (4.6.1) and U=30 m/s. The apparent confusion surrounding White and Clark's argument makes it necessary to reconsider the theoretical predictions and their applicability to the characteristics of North Pacific blocking development.

In order to obtain values for the mean winter zonal wind and vertical wind shear to be employed in the
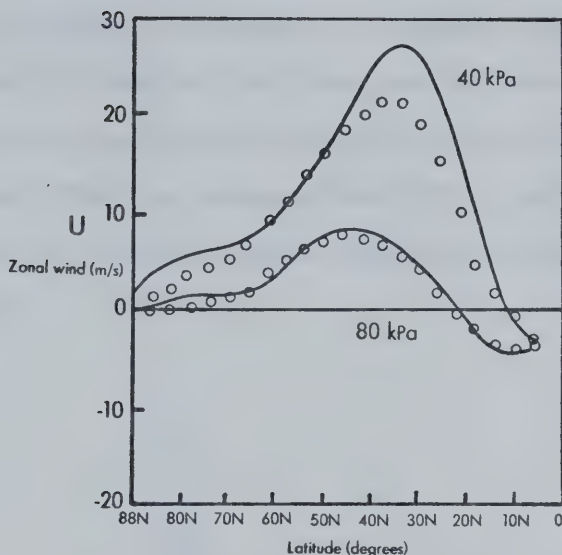
Fig. 4.14. The zonal average of the mean westerly winds for January
at 80 and 40 kPa over the Northern Hemisphere as given by Gates (1975).
The open circles are zonal averages of the observed mean wind (for
December, January, February) based on the data of Crutcher (1961).
The solid curves represent the corresponding zonal averages of the
observed geostrophic winds as based on the data of Crutcher and
Meserve (1970).

computations, use was made of the curves of Fig. 4.14 which
are taken from Gates (1975). These curves are based an
available observed wind data in the Northern Hemisphere and
those mean geostrophic zonal winds which may be calculated
from observed geopotential fields. As shown, the zonal
average of the 80 kPa westerly wind had a definite maximum
value of 8 m/s at approximately 40N to 45N. The observed
westerly wind at 40 kPa reached its maximum of just over 21

m/s at 30N to 35N although the geostrophic wind was somewhat stronger at 28 m/s. In terms of vertical wind shear across the two isobaric levels, the greatest difference in the observed mean westerlies was found to occur near 35N and was about 16 m/s. For the geostrophic zonal wind the maximum difference was slightly higher being 20 m/s at about the same latitude.

Fig. 4.15. Vertical profile of the observed mean zonal wind for the period December to February at 45N as given by Döös (1962). Values are based on the data of Crutcher (1959). Pressure (ordinate) is given as a non-dimensional variable $P = p/p_s$ where p_s = 90 kPa.
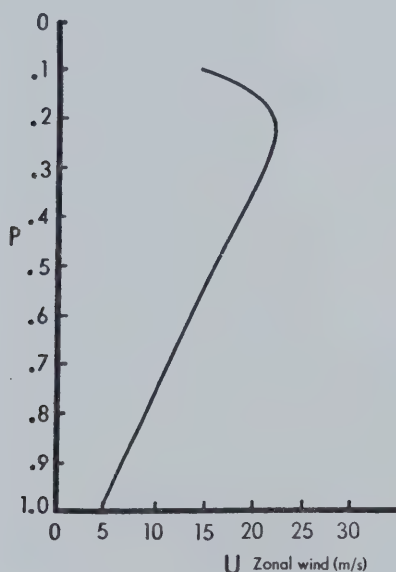
Figure 4.15 taken from Döös (1962) is also based on averaged wind data. It shows the observed zonal wind profile for the winter period December to February at a

latitude of 45N. The profile displays an almost constant
wind shear through the mid-layers of the troposphere which
translates to roughly 12 m/s over the 36 kPa interval
between P=0.8 (72 kPa) and P=0.4 (36 kPa).

Based on Figs. 4.14 and 4.15 a representative mean 60
kPa winter value of U at 45N would be approximately 13 or 14
m/s. Since observed year-to-year changes in the
autumn/winter mean wind in the lower troposphere are
typically in the order of 25% (White and Clark,1975) an
assumed range of values for U was taken to be $14 \pm (.25) \times (14)$
m/s, giving a variation from 10.5 to 17.5 m/s. The
corresponding mean vertical wind shear in the mid-
troposphere was taken as being about 7 m/s over a 20 kPa
layer. Normally the mean wind shear in the atmosphere at
mid-latitudes does not experience large fluctuations. White
and Clark have established that the year-to-year variability
in the winter value of the vertical shear for the
geostrophic wind between 100 and 70 kPa over the North
Pacific is only 5%. Since it is not inconceivable that this
also applies to the mid-troposphere a range of values was
not assigned to U_T.

It is worth noting that by using $U_T=7$ m/s the implied
mean westerly wind at 50 kPa is close to 17 m/s. If a 25%
variation is again instituted the upper estimate becomes 21
m/s which falls significantly short of White and Clark's
estimate for the mean winter westerlies of 30 m/s at this
level. General circulation studies for January, such as

those of Gates(1975) and others, typically show a simulated
local mean westerly wind maximum off the east coast of Asia
at mid-latitudes which may extend well into the North
Pacific. If correct, this implies that the winter value of
U may be slightly higher in this region than that derived
from the zonally averaged wind data. It is not likely,
however, that the increase in the mean wind over the entire
North Pacific is enough to account for the rather large
difference between the averaged values and that of 30 m/s.
It would appear from previous studies by other authors that
the lower value of near 20 m/s is more commonly used when an
estimate for the mid-latitude 50 kPa mean wind is required.

Earlier it was seen that the modelling is not
critically responsive at longer wavelengths to changes in
the mean static stability. Therefore, $\bar{\sigma}$ was held constant
at 12°C in the computations. Discussion presented in White
and Clark's study indicated that the surface sensible heat
exchange does not vary significantly during the winter
months. Hence, k_t was also given a constant value of 10^{-2}
J/(kg s °C) during the calculations.

The adiabatic version (model 1) did not predict the
possibility of stationary unstable wave growth when $U_T=7$ m/s
and U=10.5 to 17.5 m/s were used in the calculations. This
was not the case when sensible heating was incorporated.
Table 8 summarizes the phase velocity solutions of model 2
for those wavelengths with which the possibility of a
stationary unstable existed. From this table it is

Table 8.   Unstable wavelengths (L_x) and the corresponding e-folding times (t_e) for model 2 (diabatic, frictionless flow) using $U_T = 7$ m/s and $k_t = 10^{-2}$ J/(kg s °C) over a relative phase velocity range of approximately -10.5 to -17.5 m/s.

L_x (km)	t_e (days)	c_{R3} - U (m/s)
5500	6.5	-10.1
5600	6.9	-10.6
5700	7.3	-11.1
5800	7.8	-11.6
5900	8.2	-12.1
6000	8.8	-12.7
6100	9.3	-13.2
6200	9.7	-13.7
6300	10.4	-14.3
6400	10.9	-14.8
6500	11.5	-15.4
6600	12.0	-16.0
6700	12.7	-16.6
6800	13.3	-17.1
6900	14.0	-17.7

conceivable that a wave within a wavelength band of 5500 to
6800 km could undergo stationary amplification. The upper
end of this waveband would require a slightly above average
westerly wind and longer growth times while the shorter
wavelengths would give fairly rapid development with a
weaker zonal flow. In general the waveband was centered
about a value of $L_x = 6200$ km which had a relative wave speed
of about 14 m/s and an e-folding time of approximately 10
days. These values are in good agreement with
characteristic growth times of blocking (1 to 2 weeks), the
previous estimate of the mean westerlies and observations of
winter blocking ridge activity over the North Pacific.
Model 2, however, includes only sensible heating effects.
The question therefore arises as to whether incorporation of
friction in the modelling might also give similar
predictions.

Table 9 reviews the results of model 3 for $U_\tau = 7$ m/s.
The addition of friction to the adiabatic flow produced only
a very narrow band of possibilities for stationary wave
growth, ranging from 6000 to 6300 km. A look at the e-
folding times shows that, except for $L_x = 6000$ km, the growth
rates of these waves were very slow. It is, therefore,
unlikely that friction alone could result in stationary wave
amplification within the model of the same time and space
scales as atmospheric blocking.

Calculations were then done for model 4 which
incorporates sensible heat exchange and friction

Table 9. Unstable wavelengths (L_x) and the corresponding e-folding times (t_e) for model 3 (adiabatic flow with friction) using $U_T = 7$ m/s and $k_s = 4 \times 10^{-6}$ s^{-1} over a relative phase velocity range of approximately -10.5 to -17.5 m/s.

L_x (km)	t_e (days)	$c_{R3} - U$ (m/s)
5900	10.0	-10.1
6000	14.2	-10.7
6100	22.5	-11.3
6200	42.3	-11.9
6300	166	-12.6
6400	-	-13.2

simultaneously. The waveband of interest was determined as being from 5500 to 6200 km (Table 10). In almost all cases within this waveband the mean westerly wind was necessarily slightly less than its long term mean of 14 m/s for stationary wave development. The growth rates of these waves, as indicated in Table 10, were a little too slow to describe blocking development and the central value of the range of wavelengths was a rather short 5800 km. Such a wave would require a mean westerly wind of only 12 m/s to become quasistationary, but almost a month to increase its amplitude by a factor of e. The addition of frictional

Table 10. Unstable wavelengths (L_x) and the corresponding e-folding times (t_e) for model 4 using U_T = 7 m/s. Surface heating and friction constants used were k_t = 10^{-2} J/(kg m $^\circ$C) and k_s = 4 x 10^{-6} s^{-1}, respectively. The relative phase velocity range is approximately -10.5 to -17.5 m/s.

L_x (km)	t_e (days)	c_{R3} - U (m/s)
5400	14.4	-10.3
5500	16.6	-10.8
5600	19.8	-11.3
5700	23.9	-11.8
5800	29.7	-12.2
5900	38.8	-12.7
6000	55.3	-13.3
6100	86.4	-13.8
6200	228	-14.3
6300	-	-14.8

effects to the model has to a certain extent offset some of the congruity between the predictions of model 2 and observed characteristics of North Pacific blocking.

It should be cautioned that the value chosen for U_T in these calculations was critical. For instance, Table 11 is taken from model 4 under the same conditions as before except that now U_T =8 m/s. The range of possible stationary

Table 11. Unstable wavelengths (L_x) and the corresponding e-folding times (t_e) for model 4 using $k_t = 10^{-2}$ J/(kg m/s) and $k_s = 4 \times 10^{-6}$ s^{-1}. Vertical wind shear has been increased to $U_T = 8$ m/s in the calculations. The relative phase velocity range remains unchanged at roughly -10.5 to -17.5 m/s.

L_x (km)	t_e (days)	c_{R3} - U (m/s)
5500	6.2	-10.4
5600	8.7	-10.9
5700	9.7	-11.3
5800	10.8	-11.8
5900	12.2	-12.3
6000	14.0	-12.8
6100	16.1	-13.3
6200	18.7	-13.9
6300	22.3	-14.4
6400	27.4	-14.9
6500	34.2	-15.5
6600	45.7	-16.0
6700	68.6	-16.6
6800	114	-17.2
6900	424	-17.8

unstable waves was found to exist from 5600 to 6800 km. The
central value of near 6200 km had an e-folding time of
roughly 19 days and required a mean zonal wind of 14 m/s to
maintain a quasistationary position. The e-folding growth
time is slightly greater than found for atmospheric
blocking, but otherwise the values are in agreement once
more with observations of winter blocking over the North
Pacific and the estimate of the mean westerly wind speed.
Therefore, if friction is included in the modelling in
addition to sensible heating, a 1 m/s increase in the value
of U_T was required to overcome its influence. This might
suggest that atmospheric blocking occurs in the presence of
friction if the mean vertical wind shear in the mid-
troposphere is slightly above its long term mean value.
Without the presence of sensible heating, however,
stationary wave growth as predicted by the modelling is not
likely to occur. This may explain the observed decrease in
atmospheric blocking activity over the North Pacific during
the summer months since at this time sensible heat exchange
between the ocean and atmosphere is greatly reduced.

In studies where the mid-latitude standing wave problem
has been investigated by means of linear steady-state
models, it has been found that certain meridional
wavelengths for the harmonic perturbations give more
reasonable results than others when substituted into the
equations. Such was the case in the present study for
computations based on the full model version of the

equations.   Table 12 summarizes the results for three
different meridional wavelengths: L_y =60°, 90° and 120°.   The
value of U_T was again taken to be 7 m/s.   With L_y =60° the
full model does not predict the possibility of a stationary
unstable wave within the 10.5 to 17.5 m/s range selected for
the winter value of U.   When the meridional wavelength is
changed to 90° a small band of unstable stationary waves was
possible between L_x =6400 and 7000 km.   However, the growth
rates for the waves within this waveband were very slow,
being of the order of one to several months.   The last
value, L_y =120°, yielded possible stationary wave
amplification between approximately 5900 and 6700 km.   Once
again the e-folding times were fairly large, although at the
shorter end of the waveband t_e had decreased to about 3
weeks.

In general the full model, when used with U_T=7 m/s and
L_y =60° or 90°, did not satisfactorily describe winter
blocking activity over the North Pacific.   With L_y =120° the
full model predictions were similar to those of model 4
except in one significant regard, this being the value of
the central wavelength within the waveband of possible
stationary unstable amplification.   In the last column of
Table 12 this central wavelength is in the vicinity of 6300
km which is some 400 to 500 km longer than the central
wavelength predicted by model 4 (Table 10), yet the e-
folding times are comparable .   The longer 6300 km value
lies in the middle of the observed mean wavelength range of

Table 12. Unstable wave solutions for the full model using $U_T = 7$ m/s, $k_t = 10^{-2}$ J/(kg s $^\circ$C) and $k_s = 4 \times 10^{-6}$ s^{-1}. The y-axis wavelengths (L_y) are given in degrees of latitude with the origin $y = 0$ at 45N. The x-axis wavelength (L_x) interval of interest is between 5500 and 7500 km. Relative phase velocities $(c_{R3} - U)$ are given in units of m/s with e-folding times (t_e) expressed in units of days.

L_x (km)	$L_y = 60^\circ$		$L_y = 90^\circ$		$L_y = 120^\circ$	
	t_e	$c_{R3} - U$	t_e	$c_{R3} - U$	t_e	$c_{R3} - U$
5500	8.4	-6.1	10.3	-8.0	12.1	-9.0
5600	9.0	-6.2	11.3	-8.3	13.4	-9.4
5700	9.6	-6.4	12.5	-8.6	15.2	-9.7
5800	10.3	-6.5	13.9	-8.8	17.2	-10.1
5900	11.0	-6.7	15.3	-9.1	19.8	-10.4
6000	11.9	-6.8	17.3	-9.4	23.0	-10.8
6100	12.8	-6.9	19.4	-9.6	27.4	-11.1
6200	13.8	-7.1	22.0	-9.9	33.6	-11.5
6300	14.9	-7.3	25.2	-10.2	41.4	-11.8
6400	16.1	-7.5	29.5	-10.5	56.1	-12.2
6500	17.6	-7.7	35.2	-10.7	79.8	-12.6
6600	19.6	-7.8	43.4	-11.0	135	-12.9
6700	21.7	-7.9	56.0	-11.3	411	-13.3
6800	23.6	-8.1	78.3	-11.6	-	-13.6
6900	26.5	-8.2	114	-11.8		
7000	30.0	-8.4	258	-12.1		
7100	34.4	-8.5	-	-12.4		
7200	40.2	-8.6				
7300	46.4	-8.7				
7400	56.8	-8.9				
7500	72.7	-9.0				

Table 13. Unstable wave solutions for the full model with the mean vertical wind shear, U_T = 8 m/s. The respective surface constants for sensible heating and friction are k_t = 10^{-2} J/(kg s $^\circ$C) and k_s = 4 x 10^{-6} s^{-1}. The y-axis dependence is taken as being 120 degrees of latitude. Values shown are for a relative velocity range of approximately -10.5 to -17.5 m/s.

L_x (km)	t_e (days)	c_{R3} - U (m/s)
6000	9.6	-10.4
6100	10.6	-10.7
6200	11.6	-11.1
6300	12.9	-11.4
6400	14.2	-11.8
6500	16.0	-12.1
6600	17.9	-12.5
6700	20.6	-12.9
6800	23.6	-13.2
6900	27.6	-13.6
7000	32.2	-14.0
7100	39.6	-14.3
7200	51.0	-14.7
7300	67.2	-15.1
7400	97.4	-15.5
7500	173	-15.8
7600	700	-16.2
7700	-	-16.6

North Pacific blocking which is 6000 to 7000 km according to
Fig. 4.12.

Recomputed predictions for the full model with $L_y=120°$
and $U_T=8$ m/s showed an improvement in the growth rates as
was seen with model 4. As given in Table 13, all waves in
the 6000 to 7000 km range lie within the 10.5 to 17.5 m/s
range for U and could conceivably undergo stationary
amplification with e-folding times ranging from 10 days at
the lower end to roughly one month at the upper extreme.

CHAPTER 5

SUMMARY AND CONCLUSIONS

In this investigation a linear two-level baroclinic
model was formulated which incorporated a self-determining
variable static stability. The attraction of this model was
that the adiabatic-frictionless form of the equations
contained certain invariant energy and vorticity properties
which were desirable. Sensible heat exchange and frictional
effects were then introduced in the equations as
perturbation features within the steady-state current flow.

Harmonic solutions, independent of latitude or assigned
a simple meridional wavelength variation, were assumed for
the perturbation quantities. A cubic frequency equation was
obtained and solved for varying conditions of current flow.
Analysis of the resulting phase velocity response curves
showed that:

(i) adiabatic-frictionless flow yielded a band of
    unstable waves with maximum instability at
    shorter wavelengths; such flow also exhibited
    a longwave cutoff, above which wave
    amplification was not possible.

(ii) sensible heat exchange reduced the
    instability of the unstable waveband at short
    and intermediate wavelengths while increasing

the instability of longer waves.

(iii) friction diminished the instability of the
perturbation field at all wavelengths except
in two narrow regions found at the extremes of
the unstable waveband.

(iv) simultaneous inclusion of friction and
sensible heat exchange created the greatest
reduction in the amount of instability
available for short to medium length waves,
but resulted in a longwave cutoff of longer
proportions than that found with adiabatic-
frictionless flow; coincident with this the
propagation speeds of the longer unstable
waves were significantly slower.

(v) the instability and wave speeds of the long
waves increased as the meridional wavelength
of the perturbations decreased.

The stability of the perturbation field was also
subject to changes in the steady-state flow. Most notable
were the effects of using larger vertical wind shear values
and shifting the x-axis to higher latitudes both of which
created increased instability in the waves. A reduction in
the atmospheric mean stability produced more instability at
shorter wavelengths, but had appreciably less effect at
longer wavelengths.

An initial-value technique was employed to determine
the wave amplitude and phase characteristics of the various

perturbation quantities. Numerical solutions supported the findings of the stability analysis and indicated lesser wave amplification and slower wave speeds as wavelengths increased. It was also established that the thermal wave necessarily lags the stream function during unstable wave growth and that, conversely, the static stability leads the stream function wave. Maximum downward vertical velocity and the location of maximum surface heat exchange to the atmosphere were found between the ridge and the downstream trough position.

It had been suggested in a previous study by White and Clark (1975) that regional North Pacific blocking activity owed its existence to its marine environment and the presence of sensible heat flux. The present study investigated the space and time scales of the unstable baroclinic long waves which were predicted by the theory. Using representative mean winter values for the zonal wind and vertical wind shear, the numerical values indicated that stationary unstable wave amplification having similar characteristic growth rates and wavelengths as North Pacific blocking ridges was possible when sensible heating was present. Agreement between the numerical results and observed values was improved if:

(a) the vertical wind shear in the mid-
    troposphere was marginally above its long term
    mean value;

(b) the perturbation field was given a single

meridional wavelength of 120° of latitude.

In the absence of sensible heat exchange stationary wave growth was possible, but not realistic because of the extremely slow growth rates involved. Certainly such amplification would not occur on the same space or time scales as observed with blocking ridges.

The position of maximum heat exchange within the modelled atmosphere supported the spatial correlations between blocking and anomalous heat flux distributions over the North Pacific ocean found by White and Clark (1975). They found that anomalous surface sensible heating was negatively correlated with the position of a blocking ridge formation. The initial-value technique indicated that at a wavelength of 7000 km maximum perturbation heating in the surface layer of the atmosphere occurred some 50° upstream of the trough position during development, thereby putting maximum cooling just downstream of the ridge.

The concept of blocking ridge activity as a form of baroclinic instability would not seem unreasonable from the results which were found in this study. However, the theory presented can only cast inferences on the development of blocking formations. Linear perturbation theory can say very little of the ridge's ability for sustained existence without apparent further amplification. The model used in this study excluded a major mechanism for heating in the atmosphere — that of latent heat release. Further investigation is required to determine in what way this heat

source would influence the numerical predictions.
Orographic and land/sea constraints were also neglected in
the modelling. Kikuchi (1971) found in his numerical
studies that mountains and land-sea distribution played a
major role in the longitudinal position of the blocking
action, but were not necessary for the creation of blocking
waveforms. In addition, his study indicated that
numerically-simulated blocking ridges had a tendency for
longer duration if terrain effects were included in the
modelling. Additional theoretical approaches are required,
however, to substantiate the role that orographic effects
play in the scheme of blocking formations.

REFERENCES

Baur, E., 1974: Dispersion of tracers in the atmosphere and
   ocean: Survey and comparison of experimental data. _J.
   Geophys. Res., 79,_ 789-795.

Berggren, R., E. Bolin and C.G. Rossby, 1949: An aerological
   study of zonal motion, its perturbations and break-
   down. _Tellus, 1,_ 14-37.

Budyko, M.I., 1956: _The Heat Balance of the Earth_s Surface_
   (Translation prepared by the Office of Technical
   Services, U.S. Dept. of Commerce: Teplovoi balans
   zemnoi poverkhnosti, Gidrometeorologischekoe
   izdatel stvo.) Leningrad, 256 pp.

Businger, J.A., 1973: Turbulent transfer in the atmospheric
   surface layer. _Workshop on Micrometeorolgy._ Publ. by
   the American Meteor. Soc., Boston, Ma., 67-98.

Charney, J.G., 1947: The dynamics of long waves in a
   baroclinic westerly current. _J. Meteor., 4,_ 135-163.

_____, 1948: On the scale of atmospheric motions.
   Geofys. Publikasjoner, 17, 17 pp.

_____, 1959: On the theory of the general
   circulation of the atmosphere. _The Atmosphere and the
   Sea in Motion._ The Rockefeller Institute Press, 178-
   193.

_____, and N.A. Phillips, 1953: Numerical
   integration of the quasigeostrophic equations for
   barotropic and simple baroclinic flows. _J. Meteor. 10,_
   71-99.

Clark, N.E., 1967: _Report on an Investigation of Large-scale
   Heat Transfer Processes and Fluctuations of Sea-surface
   Temperature in the North Pacific Ocean._ Ph.d.
   dissertation, M.I.T., 148 pp.

Cressman, G.P., 1960: Improved terrain effects in barotropic
   forecasts. _Mon. Wea. Rev., 88,_ 327-342.

Crutcher, H.L., (ed.), 1959: _Upper Wind Statistics of the
   Northern Hemisphere._ Issued by the Chief of Naval
   Operations.

_____, 1961: _Meridional Cross-sections, Upper Winds
   Over the Northern Hemisphere._ Tech. Paper No. 41,

National Weather Records Center, Asheville, N.C.

_____, and J.M. Merserve, 1970: Selected Level Heights, Temperatures and Dew Points for the Northern Hemisphere. NAVIAR Publ. 50-1C-52, Washington, D.C.

Deardorff, J.W., 1967: Empirical dependence of the eddy coefficient for heat upon stability above the lowest 50 m. J. of App. Met., 6, 631-643.

Derome, J. and A. Wiin-Neilson, 1971: The response of a mid-latitude model atmosphere to forcing by topography and stationary heat sources. Mon. Wea. Rev., 99, 564-576.

Döös, B.R., 1962: The influence of exchange of sensible heat with the earth's surface on the planetary flow. Tellus, 14, 133-147.

Egger, J., 1976: The Linear response of a hemispheric two-level primative equation model to forcing by topography. Mon. Wea. Rev, 104, 351-364.

Gates, W.L., 1961: The stability properties and energy transformations of the two-layer model of variable static stability. Tellus, 13, 460-471.

_____, 1975: The January global climate simulated by a two-level general circulation model: A comparison with observation. J. Atmos. Sci., 32, 449-477.

Hage, K.D., 1964: Particle Fallout and Dispersion Below 30 km in the Atmosphere. Rep. SC-DC-64-1463, National Tech. Inform. Service, Springfield, Va.

Haltiner, G.J., 1967: The effects of sensible heat exchange on the dynamics of baroclinic waves. Tellus, 19, 183-198.

_____, 1971: Numerical Weather Predication. John Wiley and Sons, Inc., New York, 317 pp.

_____, and D.E. Calverly, 1965: The effect of friction on the growth and structure of baroclinic waves. Quart. J. Roy. Meteor. Soc., 91, 209-214.

_____, and F.L. Martin, 1957: Dynamical and Physical Meteorology. McGraw-Hill Book Co., New York, 470 pp.

Holopainen, E.O., 1961: On the effect of friction on baroclinic waves. Tellus, 3, 363-367.

Kikuchi, Y., 1969: Numerical simulation of the blocking

process. J. Meteor. Soc. Japan, 47, 29-45.

_____, 1971: Influence of mountains and land-sea
distributions on blocking action. J. Meteor. Soc. Japan
(special issue), 49, 564-572.

Kraus, E. and R. Morrison, 1966: Local interaction between
the sea and the air at monthly and annual time scales.
Quart. J. Roy. Meteor. Soc., 92, 114-127.

Lorentz, E.N., 1960: Energy and numerical weather
prediction. Tellus, 12, 364-373.

Lumley, J.L. and H.A. Panofsky, 1964: The Structure of
Atmospheric Turbulence. John Wiley and Sons, Inc., New
York. 239 pp.

Namias, J., 1950: The index cycle and its role in the
general circulation. J. Meteor., 7, 130-139.

_____, 1959: Recent seasonal interactions between North
Pacific Ocean waters and the overlying atmospheric
circulation. J. Geophys. Res., 64, 631-645.

Phillips, N.A., 1956: The general circulation of the
atmosphere: A numerical experiment. Quart. J. Roy.
Meteor. Soc., 82, 123-164.

Rex, D.F., 1950a: Blocking action in the middle troposphere
and its effect upon regional climate: I. An aerological
study of blocking action. Tellus, 2, 196-211.

_____, 1950b: Blocking action in the middle troposphere
and its effect upon regional climate: II. The
climatology of blocking action. Tellus, 2, 295-301.

_____, 1951: The effect of Atlantic blocking action upon
European climate. Tellus, 3, 100-112.

Rossby, C.G., 1950: On the dynamics of certain types of
blocking waves. J. Chinese Geophys. Soc., 2, 1-13.

White, W.B. and N.E. Clark, 1975: On the development of
blocking ridge activity over the Central North Pacific.
J. Atmos. Sci., 32, 489-502.

Yeh, T., 1949: On energy dispersion in the atmosphere. J.
Meteor., 6, 1-16.